BIOMIMETICS

A bioinspired revolving-wing drone with passive attitude stability and efficient hovering flight

Songnan Bai[1], Qingning He[2], Pakpong Chirarattananon[1]*

Among small rotorcraft, the use of multiple compact rotors in a mechanically simple design leads to impressive agility and maneuverability but inevitably results in high energetic demand and acutely restricted endurance. Small spinning propellers used in these vehicles contrast with large lifting surfaces of winged seeds, which spontaneously gyrate into stable autorotation upon falling. The pronounced aerodynamic surfaces and delayed stalls are believed key to efficient unpowered flight. Here, the bioinspired principles are adopted to notably reduce the power consumption of small aerial vehicles by means of a samara-inspired robot. We report a dual-wing 35.1-gram aircraft capable of hovering flight via powered gyration. Equipped with two rotors, the underactuated robot with oversized revolving wings, designed to leverage unsteady aerodynamics, was optimized for boosted flight efficiency. Through the analysis of flight dynamics and stability, the vehicle was designed for passive attitude stability, eliminating the need for fast feedback to stay upright. To this end, the drone demonstrates flight with a twofold decrease in power consumption when compared with benchmark multirotor robots. Exhibiting the power loading of 8.0 grams per watt, the vehicle recorded a flight time of 14.9 minutes and up to 24.5 minutes when equipped with a larger battery. Taking advantage of the fast revolving motion to overcome the severe underactuation, we also realized position-controlled flight and illustrated examples of mapping and surveillance applications with a 21.5-gram payload.

INTRODUCTION

Micro-aerial vehicles (MAVs), or drones, have received increasing attention and developments over the past several years. The advancements in actuation (*1*), sensing (*2*), and flight autonomy (*3*) have enabled small human-friendly aircraft to be widely commercialized and deployed (*4*–*6*). Flight, however, is energetically expensive. The issue is aggravated when the platforms are scaled down (*7*, *8*). The reduction in Reynolds numbers (*Re*) reflects the growing influence of viscous forces, adversely affecting the lift-to-drag ratio and aerodynamic efficiencies. This is exacerbated by the rise in frictional losses from transmissions, gearboxes, bearings, etc. and the decrease in power density of electromagnetic motors.

At centimeter scales, established aerial platforms capable of hovering flights are multirotor vehicles and bioinspired flapping-wing robots. When scaled down, both morphologies grossly suffer from energetic deficiencies in different manners. Small propellers, operating at fast spinning rates and elevated disk loading (ratio of thrust over the rotor disk area, *DL*), experience strong downwash and diminishing aerodynamic efficiency (*9*, *10*). In the meantime, the system efficacy benefits from the direct propulsion from motors that are mostly devoid of mechanical losses from a gearbox or transmission. On the contrary, flapping-wing MAVs, which have demonstrated sustained flight with power autonomy by leveraging unsteady aerodynamics (*11*) and relatively large planforms (*12*, *13*, *14*, *10*), have displayed aerodynamic efficiencies rivaling (*15*) or even superior (*16*) to spinning propellers. However, the sophisticated transmissions required to aggressively step down the frequency or create reciprocating wing kinematics usually incur considerable frictional losses, regardless of whether it is a gearbox needed for direct drive mechanisms (*14*) or a gear train and a crank rocker mechanism for indirect drive systems (*12*, *13*, *10*). As a consequence, the overall power efficiency of a small aerial vehicle is inevitably compromised in one way or another (*17*); flight times of small drones shorten to minutes (*7*). In an attempt to work around the limitations of each platform, researchers have proposed lighter manufacturing materials (*18*, *19*) and introduced flyers with multimodal locomotion (*20*). Surface locomotion, or perching, allows small MAVs to conduct prolonged operations while resting (*21*–*23*). These solutions, however, do not directly tackle the cause of demoted efficiency of small aircraft.

To improve the endurance of centimeter-scale MAVs, in this work, we renewed our efforts to draw inspiration from nature. Previously, fruit flies, hummingbirds, and swifts served as model organisms for piezoelectric-actuated insect-sized (*24*, *21*, *25*) and motorized robotic flappers (*12*–*14*, *10*). As briefly mentioned, unsteady mechanisms displayed by different species of insects—namely, delayed stall, rotational circulation, and wake capture (*11*)—have been exploited by several flapping-wing robots as key enhancers of aerodynamic performance. Apart from insects and avians, a large number of plants—including maple, sycamore, and spruce—produce a distinct type of natural flyers known as winged achenes (*26*) or samara. Upon falling, a samara enters autorotation and slows down the descent, increasing the dispersing distance when transported by wind, and updrafts up to several kilometers (*26*). The stable rotation of these helicopter seeds is attributed to their inertial and aerodynamic properties (*27*). Structurally, the blade of a samara essentially functions as a wing. Like insect wings, rotary seeds, varying in size from 1 cm (*26*) to 30 cm (*28*), operate at high angles of attack. A prominent leading-edge vortex (LEV) generated through autorotation has been shown to be responsible for the delayed stall and resultant elevated lift and drag (*29*). This motivates us to translate these unique passive flight principles into an aerial robot with promoted hovering efficiency.

Thus far, relatively few samara-inspired vehicles have been realized (*30*–*39*). The concept of autorotating wings for extended descent

[1]Department of Biomedical Engineering, City University of Hong Kong, Tat Chee Avenue, Hong Kong SAR, China. [2]Department of Mechanical Engineering, City University of Hong Kong, Tat Chee Avenue, Hong Kong SAR, China.
*Corresponding author. Email: pakpong.c@cityu.edu.hk

times has been directly replicated as mono-wing platforms for soft landings (*33*) and direction-controlled autorotating flight (*37*). These electroaero-mechanical devices, with samara-like wings, facilitate safe aerial deployment of sensors or lightweight payloads. Early attempts to adopt the bioinspired principle to engineer powered rotary-wing aircraft directly mimicked the monocopter design (*30*–*32*). A motorized propeller was selected for propulsion. The torque generated from the thrust device resulted in the wing rotation that produced lift. With an added servo for collective wing pitch control, akin to the flap control of conventional aircraft, the flight path was successfully manipulated. Owing to the convoluted flight mechanism and unconventional aerodynamic interactions, major efforts were required to experimentally test over 100 iterative designs to yield a vehicle with the desired passive stability and satisfactory flight performance (*31*). Flight energetics and its contributing factors of such vehicles are yet to be thoroughly modeled and investigated.

With an emphasis on energetic efficiency, we introduce a samara-like robot. With an appearance reminiscent of human-scale tip-jet helicopters (*40*–*43*) (refer to Discussion for further comparison), the 35-g vehicle features twofold rotational symmetry (Fig. 1A and Movie 1), similar to a much heavier counterpart in (*36*) and our preliminary prototype (*44*). Compared with multirotor vehicles, the proposed platform mitigates the inefficiency of small propellers with inferior power loading (thrust per unit input power, *PL*) through the augmentation of large gyrating wings for lift generation, relegating the role of propellers to the production of yaw torque that induces the wings' revolving motion. The effective power loading of the robot is, therefore, determined by the ratio of lift generated via the wings to the consumed electrical power. The sizable wings, operating at $Re \sim 2.5 \times 10^4$ at a fixed pitch angle, take advantage of unsteady aerodynamics and low disk loading for improved power loading [$PL \propto DL^{-1/2}$ when only aerodynamic power is taken into account (*9*)]. The disk loading of the proposed robot is 0.12 kg/m^2, one and two orders of magnitude lower than the 500-g revolving-wing vehicle in (*35*) and other small rotorcraft (*45*), respectively. Meanwhile, using two small motor-driven propellers instead of one motor to directly power the wings in a helicopter-like or monocopter configuration resolves the mismatch between the low torque and fast rotation of small motors and the relatively large aerodynamic load and slow rotation of enlarged wings. The symmetrical configuration, despite departing from natural winged seeds, radically simplifies the associated flight dynamics. This allows tractable models for aerodynamics, actuation efficiency, and vehicle stability to be derived and thereby enables the configuration of the revolving-wing robot powered by a pair of motor-driven propellers to be optimized for system-level power efficiency.

A flight capable prototype was fabricated, accompanied with the design guidelines to assure passive attitude stability. The resultant samara-inspired vehicle achieved stable hovering flight with the power loading more than twice as high as other aerial robots of similar weights, without the need for fast attitude feedback to stay aloft. The reported results consist of the characterization of aerodynamics and actuation efficiency, optimized vehicle configurations, dynamic and stability analysis, flight tests with detailed verification of the power efficiency, and flight endurance benchmarked against conventional

Movie 1. Overview of the bioinspired revolving-wing drone.

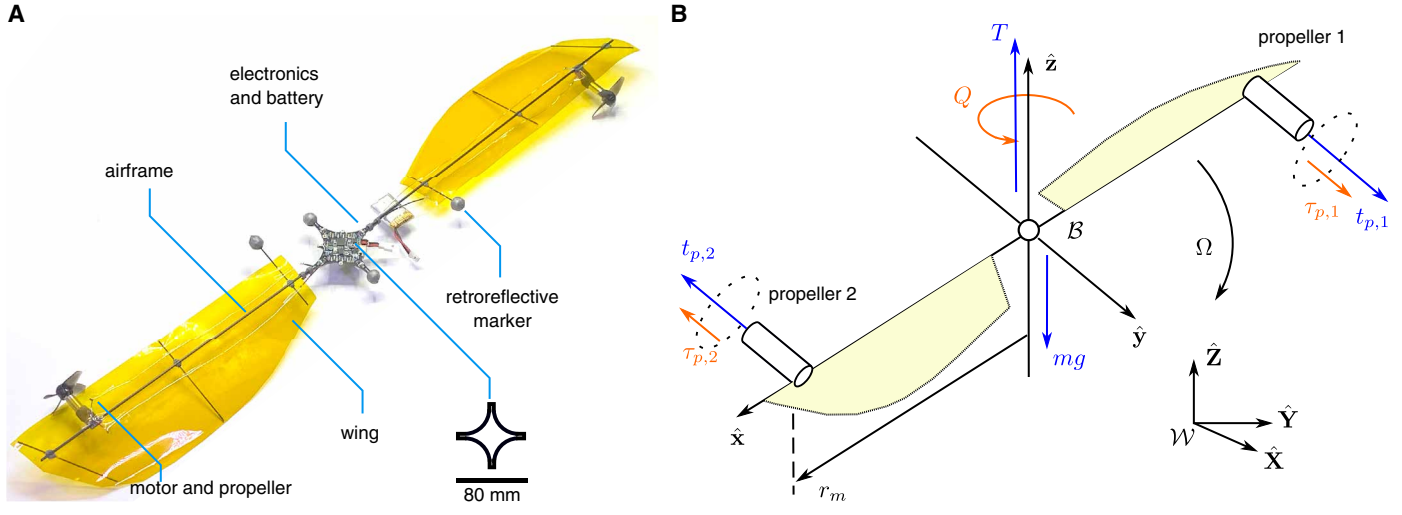

Fig. 1. Design and working principles of the propeller-driven samara-inspired robot. (**A**) Photography of the revolving-wing robot. The scale bar illustrates the size of the flight control board (80 mm). (**B**) Schematic diagram of the robot depicting the nominal flight dynamics and the definition of coordinate frames. The blue and orange arrows designate forces and torques, respectively.

rotorcraft and motorized flapping-wing vehicles. The discussion of systemic power consumption and example applications are provided.

RESULTS

Robot design and flight principles

To create an aerodynamically efficient robot that leverages a stable LEV, we use a bioinspired approach. Rather than directly mimicking the geometry of maple seeds with mono-wing designs (*31*–*34*), the 35.1-g samara-inspired robot features oppositely placed flat wings, two horizontally directed motor-driven clockwise-spinning propellers, and centrally located flight electronics (Fig. 1A). The symmetric design guarantees that the robot stays upright in hovering flight, while the horizontal propeller placement ensures that they primarily take the role in the torque generation. The conditions lead to a tractable dynamic model suitable for design optimization, stability analysis, and flight control.

To stay aloft, the vertical thrust T is produced by the revolving wings, countering the gravity (Fig. 1B). In operation, the thrust produced by two motor-driven propellers (t_{p1}, $t_{p,2}$) located at the distance r_m from the robot's vertical axis ($\hat{\boldsymbol{z}}$) results in net yaw torque of $2t_p r_m$, inducing the rotating motion. In equilibrium, the wings gyrate at a steady angular velocity $\boldsymbol{\Omega}$, experience aerodynamic drag torque Q, and collectively generate vertical thrust T, leading to the balanced conditions

$$T = mg \text{ and } Q = 2t_p r_m \tag{1}$$

where mg is the weight of the vehicle and $t_{p1} = t_{p2} = t_p$. To achieve high energetic efficiency, it is vital to model the aerodynamic performance of the wings and their interaction with the propelling thrusts.

Revolving-wing aerodynamics

On the one hand, the revolving wings can be regarded and modeled as an actuator disk. On the other hand, the relatively low angular velocity ($\boldsymbol{\Omega}$) implies an intermediate flow regime (Reynolds number $Re \sim 2.5 \times 10^4$). This allows the wings with relatively high angles of attack and low aspect ratios to form a stable LEV enjoyed by flapping-wing MAVs (*13*, *1*, *14*, *10*, *46*), amplifying the force coefficients (*47*–*49*). To capture unsteady mechanisms, the quasi-steady model and blade element theory are adopted to describe elemental lift (F_L) and drag (F_D) along the wing element dr at the radial position r from the revolving axis (fig. S1A)

$$\mathrm{d}F_{L/D}(r) = \frac{1}{2}\rho C_{L/D}(\alpha(r))\, c_h(r)\, V^2(r)\, \mathrm{d}r \tag{2}$$

where ρ is the air density, r is the distance from the rotational axis ($\hat{\boldsymbol{z}}$), $\alpha(r)$ is the local geometric angle of attack defined as the angle between the local airflow direction and the chord line of the wing (cf. the effective angle of attack α_e, which is defined as the angle between the local airflow direction and the zero-lift line of the wing; see fig. S1B), $c_h(r)$ is a wing chord function, $V(r)$ is the relative local air speed, and $C_{L/D}(\alpha)$ is either lift or drag coefficient. The angle of attack α differs from the wing pitch angle β owing to the induced velocity. In addition, unlike aircraft airfoils, the presence of LEVs and large angles of attack suggests that the force coefficients follow the relationship previously established by studies on quasi-steady models of flapping and revolving wings at low-to-intermediate Reynolds numbers (*47*, *29*, *49*): $C_L(\alpha) = C_{L,0} + C_{L,1} \sin(2\alpha)$ and $C_D(\alpha) = C_{D,0} + C_{D,1}(1 - \cos(2\alpha))$.

In the revolving motion, each elemental blade encounters different air velocities as well as angles of attack, resulting in different elemental aerodynamic lift and drag. As detailed in Materials and Methods and fig. S1, the projection of these force elements onto the robot frame yields elemental thrust dT and torque dQ. To eliminate the dependence on $V(r)$, the general momentum theory (MT) provides additional expressions of dT and dQ by taking into consideration the following: (i) axial and tangential airspeeds of the helical wake and relating them to the revolving rate $\boldsymbol{\Omega}$ and (ii) tip loss effects (see Materials and Methods) (*50*–*53*). Integrating the results from MT with those from blade element method (BEM) yields

$$T = C_T \Omega^2 \text{ and } Q = C_Q \Omega^2 \tag{3}$$

where the thrust and torque coefficients (C_T and C_Q) are functions of the wing chord profile $c_h(r)$ and the wing pitch angle β.

Experiments were conducted to verify and identify the model parameters with various shapes and sizes of wings at the scale of interest (~10 cm). We fabricated six pairs of flat lightweight wings from polyimide film and carbon fiber rods (fabrication procedures are described in Materials and Methods). The aspect ratios of the sample wings range from 1.6 to 5.7 (Fig. 2A). Both tapered and rectangular profiles were included to capture the tip loss factor.

A revolving platform consisting of a servo motor and a force/torque transducer (see Fig. 2B and Materials and Methods) was constructed for the parameter identification. Each pair of wings was tested at four- or five-blade pitch angles (between 0° and 50°). The combination of six wings at various pitch angles produces the total of 29 wing configurations. We took measurements of thrust and torque of each wing configuration at four to six angular velocities, up to 14π rad/s, to evaluate 29 pairs of empirically fitted thrust and torque coefficients (C_T and C_Q; see fig. S2). A single set of force coefficients, $\{C_{L,0}, C_{L,1}, C_{D,0}, C_{D,1}\}$, was then determined by minimizing the difference between the empirically fitted and modeled thrust and torque coefficients (Fig. 2C) as detailed in Materials and Methods.

The model predictions of thrust and torque coefficients of six sample wings at various wing pitch angles calculated from a set of best-fitted lift and drag coefficients (fig. S3) reveal agreement with empirical measurements (Fig. 2C and fig. S2). The thrust coefficients increase with the wing pitch angle up to ≈45°, corresponding to the angles of attack (computed at mid wing) of near 35° (figs. S4 and S5). The elevation of both thrust and torque coefficients at large wing pitch angles corresponds to amplified lift and drag coefficients at high angles of attack, suggesting the presence of a rotation-induced LEV that prevents stall (*29*). The model predicts the peak lift coefficient of 1.80 (fig. S3), comparable with flapping (*54*) and revolving (*55*) insect wings with similar aspect ratios (~3) and Reynolds numbers (~10^4). To assess aerodynamic efficacy, we inspect the glide ratio (C_L/C_D) and power factor ($C_L^{3/2}/C_D$). The power factor is a dimensionless ratio of lift to aerodynamic power, indicating the efficiency of endurance (*48*). The results reveal the maximum glide ratio and power factor of ≈6.7 and ≈5.1 (fig. S3), slightly higher than the reported values of revolving dynamically scaled insect wings at Reynolds number 1.4×10^5 (*55*), possibly due to the slightly larger Reynolds numbers (up to ~2.5×10^4) at the test conditions. Nevertheless, the enhanced aerodynamic performance does not immediately

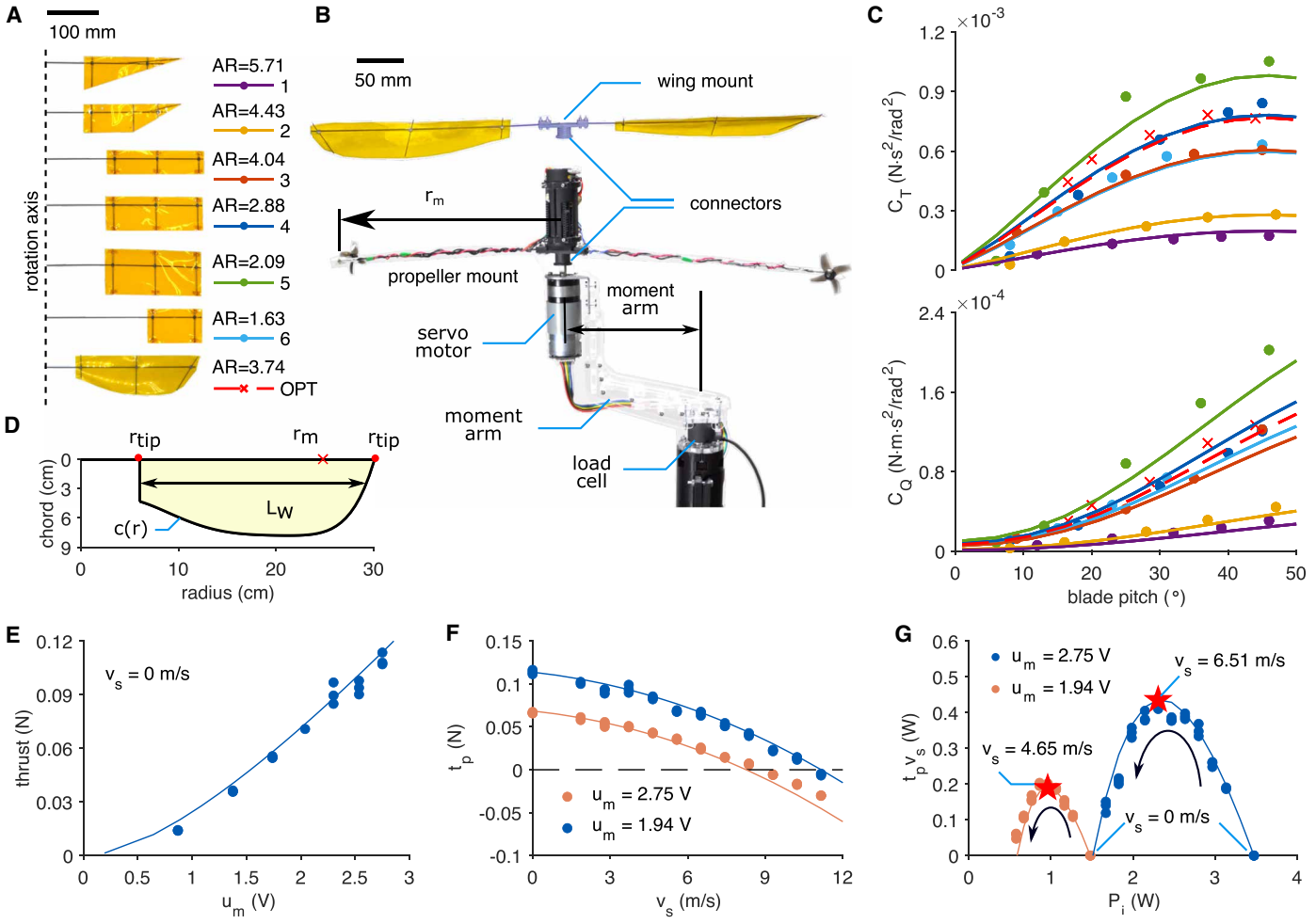

Fig. 2. Characterization of revolving-wing aerodynamics and power consumption of motor-driven propellers in the presence of nonzero free-stream velocity. (**A** to **D**) Experimental results and optimization of revolving-wing aerodynamics. (A) Photographs of seven tested wings [with the optimized wing (OPT) included] and corresponding aspect ratios. (B) Experimental setup for testing the wings and propellers. Wing mount and propeller mount are replaceable parts and can be mounted on the servo motor for different objectives. (C) Model identification results of the wing aerodynamics. The plots display the model predictions (line) and experimental measurements (points) of C_T and C_Q at different blade pitch angles [refer to (A) for the legends]. (D) Wing profile and location of the motor for the optimized configuration. The corresponding optimal blade pitch angle is 19.5° (not shown). (**E** to **G**) Characterization of the motor-driven propellers in the presence of free-stream flow. Dots represent empirical measurements, and lines represent fitted models. (E) The relationship between the propelling thrust and driving voltage in the absence of the free-stream velocity. (F) Propelling thrust plotted against the incoming free-stream velocity. Two driving voltages were tested. (G) The plot shows the mechanical output power of the motor-driven propeller operating at various free-stream velocities versus the electrical input power. The output power of the motor-driven propeller serves as the mechanical input power of the revolving wings. Two colors designate two driving voltages.

translate to an energetically efficient vehicle because it does not take into account the actuation efficiency and related flight mechanism.

Motor-driven propellers

The samara-inspired robot is powered by a pair of motor-driven propellers. In the proposed design (Fig. 1), two propellers collectively generate yaw torque to counter the drag from the revolving wings. To reduce power consumption, it is necessary to comprehend the coupled relationship between the actuation and lift and drag. Similar to the rotating wings, the aerodynamics of the propellers are described by MT and BEM with some modifications.

By applying a few simplifying assumptions on the blade geometry and force coefficients to BEM as described in Materials and Methods, we obtained a lumped propeller model (*56*). In this formulation, the vehicle's yaw rotation is interpreted as the translational motion of the propellers (located at a distance r_m from the robot's yaw axis) along their axial direction, attributing to the free-stream velocity $v_s = \Omega r_m$ perceived by the rotors. The nonzero free-stream velocity directly affects the propeller's thrust, torque, and power. Furthermore, because the rotational wake is omitted from the lumped parameter model, an empirically determined induced power factor κ_p is introduced to account for the energy dissipated by wake rotation. When incorporated with MT, the propeller's thrust and torque coefficients, defined as $c_T = t_p/\omega^2$ and $c_\tau = \tau_p/\omega^2$, in which τ_p is propeller's drag torque and ω is the rotor angular speed, are no longer constant but functions of $v_s/(r_p\omega)$ or $\Omega r_m/(r_p\omega)$, where r_p denotes the radius of the propeller.

In terms of actuation, in steady states, the rotor torque τ_p is in balance with the torque provided by the DC motor as dictated by the equation $\tau_p = k_m(u_m - k_m\omega)/R_m$ when k_m is a motor constant, R_m

is the motor's internal resistance, and u_m is the driving voltage. Given the motor parameters, we are able to predict the propeller's thrust t_p and its spinning rate ω from the input voltage u_m and free-stream velocity v_s (details in Materials and Methods). That is, the combination of the lumped model and motor equation ultimately produces a deterministic function $t_p = f_p(u_m, v_s)$.

To validate the lumped parameter model, particularly in the presence of nonzero free-stream velocity, the motor parameters were first identified, followed by another set of experiments to determine the propeller's parameters as they appear in the lumped model. The motor parameters k_m and R_m were determined with a linear regression from current and angular rate measurements obtained when the motor was driven at different voltages in varied experimental conditions as described in Materials and Methods. Next, a pair of motor-driven propellers (40-mm four-blade) were mounted on a servo motor and a load cell as depicted in (Fig. 2B). In this setup, the propellers underwent a rotational motion that brought an approximately linear translation along the propeller's axis, equivalent to a nonzero free-stream flow velocity, resembling the operational conditions of the propellers on the samara-inspired robot. The vertical torque measured by the load cell can be readily converted to the propellers' thrust, while the free-stream velocity is governed by the servo motor. The measurements were taken at (i) seven voltages with zero free-stream velocity and (ii) two voltage values (u_m = 1.94 and 2.75 V), each with 11 free-stream velocities up to over 10 m/s. A total of 95 data points with the maximum thrust of 0.12 N were recorded for the fitting of the propeller's coefficients as detailed in Materials and Methods. The thrust predictions fit the experimental data well with an average root mean square error (RMSE) of 2.6 mN (Fig. 2, E and F). The results reveal a reduction in the propeller's thrust as the free-stream velocity v_s increases when the driving voltage remains constant. On the basis of the measurements and the developed model, we further inspect the ratio of the mechanical output power (the product of thrust and the translational speed or free-stream velocity, $t_p v_s$) to the estimated input electrical power P_i. Because the output power of the motor-propeller subsystem can be regarded as an input power of the revolving wings, the power ratio indicates the efficiency of the motor-propeller pair in the context of the revolving-wing vehicle. Initially, the output power $t_p v_s$ grows as v_s rises. However, as the reduction in t_p (Fig. 2F) becomes increasingly dominant, the output power begins to drop. The presence of the peaks of the power ratios (Fig. 2G) implies the existence of an optimal operating condition, prompting a search for a suitable vehicle configuration. Without such consideration, aerodynamically efficient wings alone would not immediately lead to a vehicle with superior overall flight efficiency.

Design optimization for flight endurance

The developed aerodynamic and actuation models capture the energetics of steady-state flight. The tailored symmetric vehicle configuration gives rise to tractable analytical models with predictive abilities, rapidly accelerating the vehicle optimization process by eliminating the need to experimentally characterize a large number of prototypes as performed in (*31*, *32*, *12*). This engineering-centric solution offers an intelligent alternative to direct biomimetic designs (*33*).

To make use of the preceding outcomes, we opted to enhance the flight endurance by minimizing the power the robot requires for hovering ($T = mg$). The task is to seek the optimal wing geometry and propellers' location under certain constraints. This is carried out by parameterizing the wing profile and propellers' placement by a set of 11 design parameters: Θ consisting of the propeller's radial location r_m, wing pitch angle β, wing root r_{root}, and wing tip r_{tip} positions, and seven variables defining the chord function as described in Materials and Methods. The optimization, based on the separately identified wing and actuation models, neglects the possible aerodynamic interactions between the wings and the propellers. The task is mathematically formulated as

$$\Theta^* = \arg\min_{\Theta, u_m} P_i(\Theta, u_m) \text{ subject to } T(\Theta, u_m) = m(\Theta)g \quad (4)$$

and two other practical constraints related to (i) the maximum platform size and (ii) the upper bound of the wing aspect ratio as detailed in Materials and Methods. The limit on the vehicle size is imposed owing to scaling effects that favor large planform areas and lower disc loading as manifested by MT (*56*, *8*). The conditioning on the aspect ratio is to warrant the stability of LEV (*55*, *49*).

The parameter search was achieved with the Nelder-Mead algorithm. Different initial estimates were explored to avoid local minima. The algorithm generated a vehicle configuration with an estimated mass of 33.2 g with a wing semispan of 300 mm that consumes 3.48 W in hover with the nominal voltage u_m = 2.53 V (Fig. 2D). The motors and propellers are positioned 247 mm from both sides of the center of rotation. The resultant wing with an aspect ratio of 3.7 and a pitch angle of 19.5° features a relatively narrow chord near the root and a tapered tip as a result of the tip loss. Despite the variation in the local free-stream velocity, during hover, the local angle of attack of the derived wing profile is anticipated to be approximately uniform across the entire wing at $\alpha \approx 11^\circ$ (fig. S5), near the angle that displays a peak in power factor indicated by the model of lift and drag coefficients (fig. S3). As a consequence, the sectional lift is maximum near the wing tip (fig. S5). These characteristics are vastly distinct from those exhibited by autorotating plant seeds that operate at generally greater angles of attack (Reynolds numbers of ~10^3) (*29*). This is because autorotating seeds exploit a relatively compact LEV at extremely high angles of attack toward the seeds to amplify lift and prolong descent time for successful dispersion. The associated increase in drag at high angles of attack promotes the gyration and does not adversely affect its lift generation. The outcome illustrates the insights gained from the engineering design perspective.

Analysis of flight dynamics and passive attitude stability

Reminiscent of autorotating flights of winged seeds (*29*, *27*), existing revolving-wing robots exhibit different degrees of inherent attitude stability in flight (*31*–*33*, *44*). That is, samara-inspired vehicles stay approximately upright in the absence of feedback. The passive attitude stability, also displayed by most fixed-wing bird-like aircraft (*57*, *58*), is in sharp contrast to small multirotor vehicles (*59*, *7*) and tailless flapping-wing robots (*12*, *60*, *1*, *14*), unless large aerodynamic dampers are incorporated (*61*, *62*).

Still, the dynamics and stability of powered samara-inspired vehicles are different from those of autorotating winged seeds or other unpowered platforms (*26*, *31*, *37*), which partially rely on the relative upward airstream. A numerical model (*63*) and experimental findings (*26*, *31*, *64*, *65*) signify the influence of the mass distribution on stable autorotation. For powered revolving-wing vehicles, the preference for the lower center of mass with respect to the center of pressure for attitude stability is acknowledged but has not been comprehensively modeled or systematically verified in (*31*, *34*–*36*).

To elucidate the observed behavior and derive the design principles for realizing attitude stability, the flight dynamics of the proposed robot is investigated (see the Supplementary Materials for details). Even near hovering, the wings travel through the air at a notable speed because of the gyrating motion, creating non-negligible additional aerodynamic interactions that affect the translational and rotational dynamics of the vehicle. In addition, the continuous revolving motion renders models applied to conventional rotorcraft cumbersome for describing the robot's attitude. As a consequence, we focus on the inclination of the robot's vertical axis ($\hat{\mathbf{z}}$ in Figs. 1B and 3A) and partially discard the swiftly varying yaw angle by treating the near-hovering robot as an axisymmetric disk with the moment of inertia equal to diag(I_d, I_d, I_z) rotating about its $\hat{\mathbf{z}}$ axis at the rate of Ω_z. This yaw rate is primarily determined by the interplay of the sum of propelling thrust and the torque from the rotating wings as

$$I_z\dot{\Omega}_z = -r_m(t_{p,1} + t_{p,2}) - C_Q\Omega_z|\Omega_z| \quad (5)$$

In the meantime, the attitude of the disk-like robot, as seen in the inertial frame ($\hat{\mathbf{X}}\,\hat{\mathbf{Y}}\,\hat{\mathbf{Z}}$), is captured by the coordinates $\{\xi_x, \xi_y\}$ defined as the rotation angles of $\hat{\mathbf{z}}$ from $\hat{\mathbf{Z}}$ with respect to $\hat{\mathbf{X}}$ and $\hat{\mathbf{Y}}$ as $\hat{\mathbf{z}} \approx [\xi_y, -\xi_x, 1]^T$ for $\xi_x, \xi_y \ll 1$ (Fig. 3A). The translational motion of the robot is subject to drag proportional to the velocity perceived in the body frame. The vertical component of the acceleration is chiefly governed by the thrust generated by the revolving wings through Ω_z and its weight as

$$m\ddot{z} = (t_{p,1} - t_{p,2})\xi_x + C_T\Omega_z^2 - b\dot{z} - mg \quad (6)$$

where b is the linear drag coefficient and the differential thrust is the contribution from the propellers projected onto the vertical axis. The lateral acceleration of the robot is subject to the drag and the propelling thrust $C_T\Omega_z^2$ projected onto the horizontal directions as

$$m\begin{bmatrix}\ddot{x}\\ \ddot{y}\end{bmatrix} = -b\begin{bmatrix}\dot{x}\\ \dot{y}\end{bmatrix} + C_T\Omega_z^2\begin{bmatrix}\xi_y\\ -\xi_x\end{bmatrix} + (t_{p,1} - t_{p,2})\begin{bmatrix}-\sin\psi\\ \cos\psi\end{bmatrix} \quad (7)$$

where ψ is the instantaneous yaw angle of the robot (Fig. 3A). It can be seen that the translational motion is tightly coupled with the robot's inclination, ξ_x, ξ_y. As derived in the Supplementary Materials, the reduced attitude dynamics follows

$$I_d\begin{bmatrix}\ddot{\xi}_X\\ \ddot{\xi}_Y\end{bmatrix} + I_z\Omega_z^*\begin{bmatrix}\dot{\xi}_Y\\ -\dot{\xi}_X\end{bmatrix} = \sum\tau \quad (8)$$

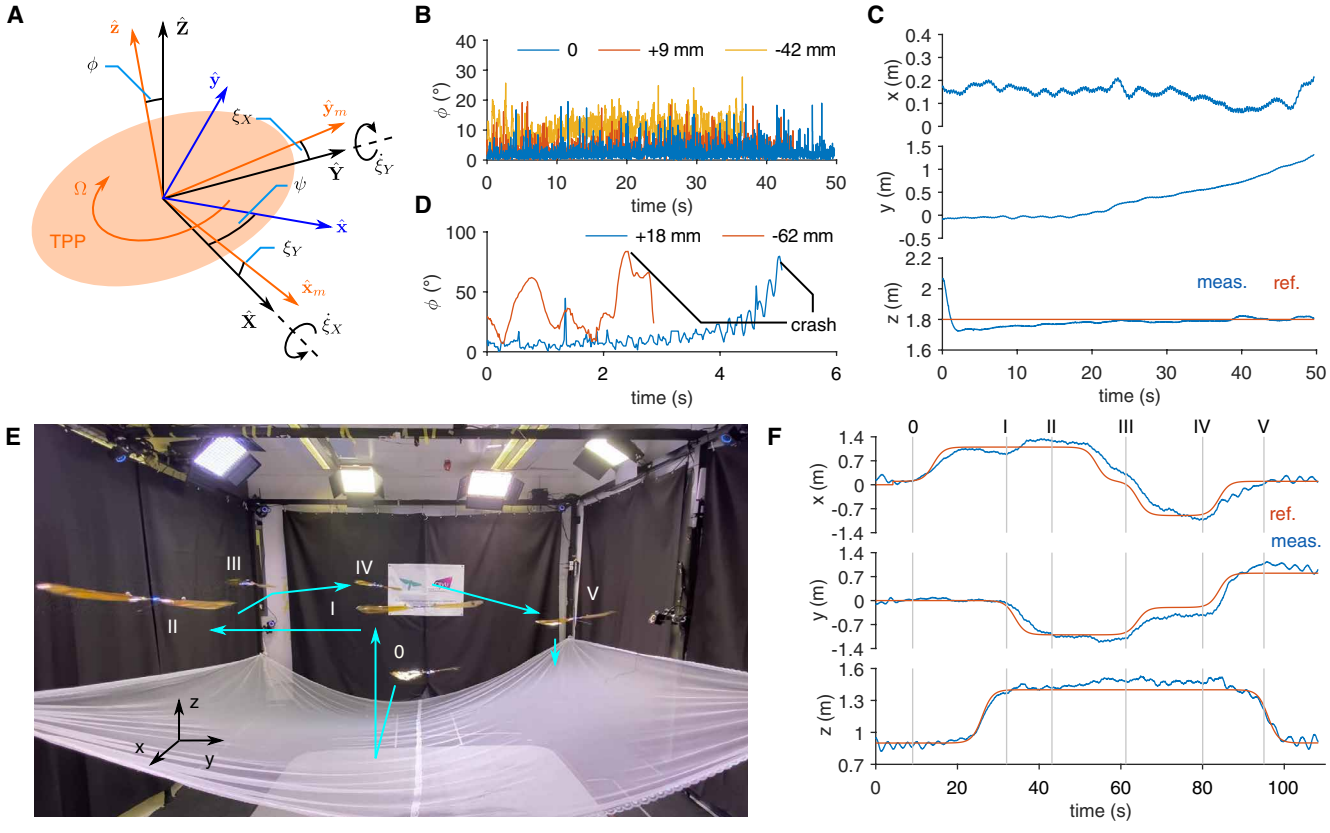

Fig. 3. Reduced attitude dynamics, passive stability, and position-controlled flight. (**A**) Definitions of the inertial frame, body-fixed frame, and the auxiliary frame introduced to describe the orientation of $\hat{\mathbf{z}}$. The frame origins are offset for improved clarity. Only the flight position was controlled. (**B**) Time course of the inclination angle ϕ, defined as the angle between $\hat{\mathbf{z}}$ and the vertical axis, from an open-loop flight. The well-tuned robot displays passive attitude stability (movie S1). (**C**) Flight trajectory of the stable robot from the open-loop flight. (**D**) Inclination angle ϕ of the robot with displaced center of mass taken from two open-loop flights. The battery was relocated downward by 3 cm (red, movie S1) or upward by 1 cm (blue, movie S1). (**E**) Composite image capturing the trajectory of the robot in a closed-loop trajectory-tracking flight (movie S1). (**F**) Trajectory of the robot with respect to the reference in a position-controlled flight.

where $\sum\tau$ is the total torque experienced by the robot expressed in the inertial frame, contributed by the generated thrusts from both propellers ($t_{p,1}$ and $t_{p,2}$) and aerodynamic forces

$$\sum\tau = \kappa(t_{p,1} - t_{p,2})\begin{bmatrix}-\sin\psi\\ \cos\psi\end{bmatrix} - c\begin{bmatrix}\dot{\xi}_x\\ \dot{\xi}_y\end{bmatrix} + bl_{cp}\begin{bmatrix}\dot{y}\\ -\dot{x}\end{bmatrix} - \gamma\Omega_z^*\begin{bmatrix}\dot{x}\\ \dot{y}\end{bmatrix} + \dot{z}\Gamma_\tau\begin{bmatrix}\dot{\xi}_x\\ \dot{\xi}_y\end{bmatrix} \quad (9)$$

where κ is the effective propeller's thrust-to-torque coefficient (e.g., $\tau_{p,1} = \kappa t_{p,1}$), c is a positive lumped coefficient for the rotational drag, l_{cp} is the vertical offset between the center of mass of the robot and center of pressure of the revolving wings ($l_{cp} > 0$ indicates that the center of mass is located below the center of pressure), γ captures the torque attributed to the dissymmetry of lift (or differential lift) experienced by the advancing and retreating of the spinning wings in translation (*66*, *67*), and $\Gamma_\tau = \Gamma_\tau(\psi, l_{cp}, \gamma, \Omega_z)$ is a 2×2 matrix described in the Supplementary Materials. Together, Eqs. 5 to 9 present the coupled behaviors of the robot's translational and attitude dynamics near a hovering state.

To characterize the open-loop stability, we inspect circumstances where only the nominal commands $t_{p,1} = t_{p,2} = ((C_Q/C_T)mg)/2r_m$ are applied. The yaw dynamics described by Eq. 5 settles to $\Omega_z = \Omega_z^* = -\sqrt{mg/C_T}$ and $T = mg$ (using Eqs. 1 and 3), approximately stabilizing the altitude to $\dot{z} = 0$ (Eq. 6). The reduced attitude and lateral dynamics subsequently simplify to

$$m\begin{bmatrix}\ddot{x}\\ \ddot{y}\end{bmatrix} + b\begin{bmatrix}\dot{x}\\ \dot{y}\end{bmatrix} - mg\begin{bmatrix}-\xi_y\\ \xi_x\end{bmatrix} = 0 \quad (10)$$

and

$$I_d\begin{bmatrix}\ddot{\xi}_x\\ \ddot{\xi}_y\end{bmatrix} + I_z\Omega_z^*\begin{bmatrix}\dot{\xi}_y\\ -\dot{\xi}_x\end{bmatrix} + c\begin{bmatrix}\dot{\xi}_x\\ \dot{\xi}_y\end{bmatrix} - bl_{cp}\begin{bmatrix}\dot{y}\\ -\dot{x}\end{bmatrix} + \gamma\Omega_z^*\begin{bmatrix}\dot{x}\\ \dot{y}\end{bmatrix} = 0 \quad (11)$$

Equations 10 and 11 present two tightly coupled second-order subsystems, of which the analytical stability conditions become increasingly intractable. To gain some apprehension on dominating effects that affect the stability of the robot for the vehicle design purposes, we leverage the fact that for the robot with sizeable wings and rapid yaw rotation, the aerodynamic forces dominate the translational dynamics (further discussion in the Supplementary Materials). Neglecting the inertia term in Eq. 10, the two subsystems combine into

$$I_d\begin{bmatrix}\ddot{\xi}_x\\ \ddot{\xi}_y\end{bmatrix} + I_z\Omega_z^*\begin{bmatrix}\dot{\xi}_y\\ -\dot{\xi}_x\end{bmatrix} + c\begin{bmatrix}\dot{\xi}_x\\ \dot{\xi}_y\end{bmatrix} - l_{cp}mg\begin{bmatrix}\xi_x\\ \xi_y\end{bmatrix} - \frac{\gamma\Omega_z^* mg}{b}\begin{bmatrix}\xi_y\\ -\xi_x\end{bmatrix} = 0 \quad (12)$$

According to the Routh-Hurwitz criterion, the requirements for passive attitude stability of the system described by Eq. 12 are

$$-\frac{I_z^2\Omega_z^2 + c^2}{mgI_d} + \frac{\gamma I_z\Omega_z^2}{bc} < l_{cp} \text{ and } -\frac{I_z\Omega_z^2\gamma}{bc} + \frac{I_d mg\Omega_z^2\gamma^2}{b^2c^2} < l_{cp} \quad (13)$$

Recall that because all parameters, except l_{cp}, are strictly positive, the criteria imply that stability is attained as long as the center of mass is sufficiently lower than the center of pressure. Furthermore, the damping coefficients c and b contribute favorably to the passive stability, whereas the dissymmetry of lift, as described by γ, effectively brings about the destabilizing effect for open-loop flight. The stability criteria can be achieved when l_{cp} is in a suitable range and the damping components dominate.

The finding is largely in agreement with previously reported experimental results of robots with similar flight principles (*31*, *67*, *44*). In practice, nevertheless, an attempt to lower the center of mass to secure passive stability by increasing l_{cp} would likely simultaneously raise the inertia I_d. This turns out to oppose the stability condition suggested by Eq. 13. That is, depending on several factors (such as b, c, and m) combined, there likely exists only a limited range of l_{cp} that results in passive attitude stability.

Flight-capable prototype, stability tests, and position-controlled flights

The flight-capable prototype was constructed according to the optimized profile, based on the fabrication techniques used in the early iteration of the revolving-wing robot (*44*). The robot is made up of four primary components: the airframe, wings, a pair of motors and propellers, and flight electronics, as presented in Fig. 1A.

The airframe was constructed from two carbon fiber rods with 1.8-mm diameter and a flight control board [Bitcraze, Crazyflie 2.1; (*68*)] affixed together by three-dimensional (3D)–printed connectors (Gray resin, Form 3, Formlabs) (refer to Fig. 4A). The open-source control board, containing redundant features, such as additional motor drivers, was selected to accelerate the development. To minimize the weight, the wings were made from 75-μm-thick polyimide film (Kapton, Dupont) and cut to the desired geometry using a CO_2 laser cutter (Epilog, Mini 24). The polyimide wings are reinforced by the wing ribs (carbon fiber rods with 1.2-mm diameter) and rigidly mounted on the airframe via 3D-printed connectors. The geometry of the printed connectors dictates the tilted angle of the ribs and the wing pitch angle (Fig. 4A). Custom jigs were used to assure the desired wing pitch angles and the flatness of the surface of the wings (see Fig. 4, B and C). All parts were glued together using cyanoacrylate adhesives and epoxy resin.

To validate that the wings can be regarded as rigid flat plates as modeled, a wing rigidity test was carried out (detailed in the Supplementary Materials). We visually inspected the deformation of the wings in rotation and compared the aerodynamic force and torque (T and Q from Eq. 3) of the polyimide wings and a pair of rigid wings made of fiberglass. The video footage verifies negligible wing deformation when they rotated at the anticipated revolving speed (see Fig. 4D and movie S4), attributable to the structural support provided by the wing ribs and the low wing loading ($\approx$0.1 g/cm^2 at Ω = 18.8 rad/s). The force and torque coefficients (C_T and C_Q) of the two wing types at $\Omega < 30$ rad/s are nearly identical (the differences in C_T and C_Q are less than 1% and 2%, respectively; fig. S15). In contrast, at spinning rates markedly faster than the flight condition, structural bending and wing flapping motion became evident (fig. S13 and movie S4).

For actuation, we used 20-mm-radius four-blade propellers ($2 \times$ 0.83 g) and 7 mm–by–20 mm coreless DC motors (2×3.72 g). Using the built-in speed controller on the flight control board (6.36 g) and a 250-mAh single-cell Li-ion battery (8.00 g), the propeller can generate steady-state thrust up to $\approx$150 mN in the absence of free-stream velocity. The flight-capable prototype weighs 33.0 g, almost equal to 33.2 g predicted by the design optimization process. After attaching four markers for the motion capture cameras, the weight increases to 35.1 g.

To achieve position-controlled flight, a customized flight controller is developed. The proposed control framework for the samara-inspired robot is markedly different from strategies applied

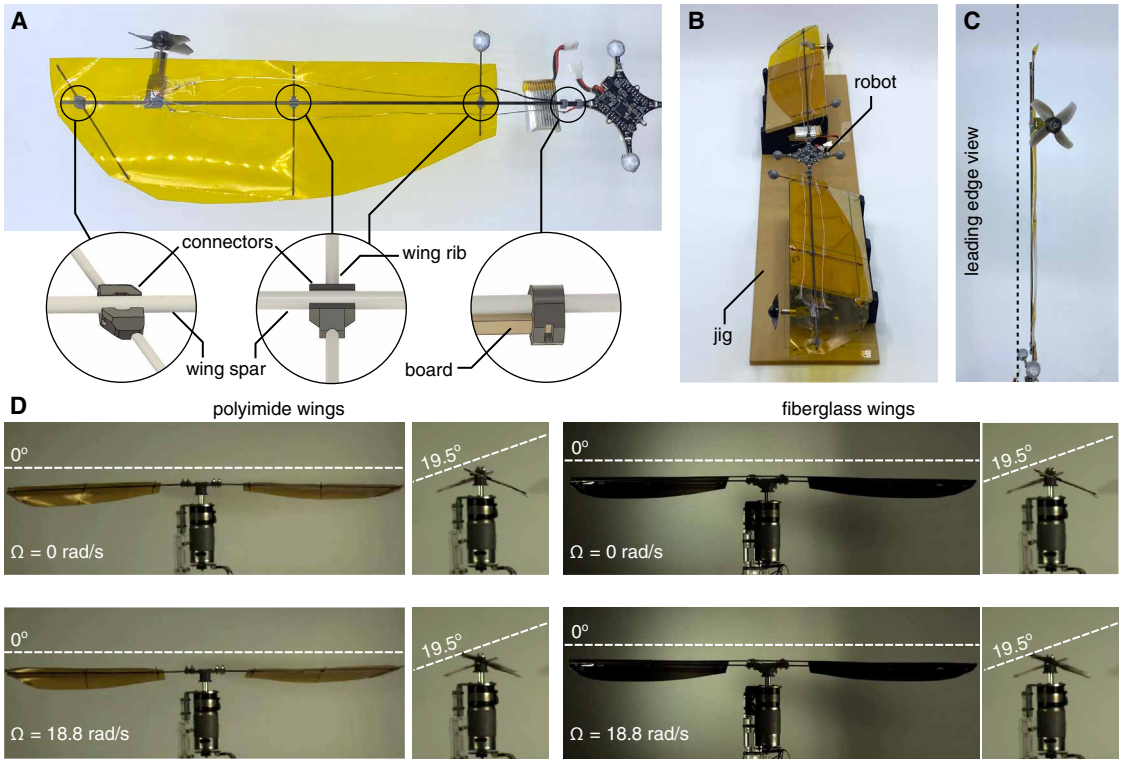

Fig. 4. Robot fabrication and wing rigidity analysis. (**A**) Close-up view of the wing showing the components. (**B**) Robot on the custom jig during the assembly process. (**C**) Wing as viewed from the leading edge. (**D**) Comparisons between the polyimide wings and fiberglass wings in the rigidity test, including snapshots from high-speed videos of the wings driven by the revolving platform at the speed of 0 and 18.8 rad/s (the revolving speed of the robot in hovering).

to multirotor vehicles owing to two primary reasons. The first is the difference in the flight principles, and the second is the degree of underactuation of the two-rotor flyer.

The devised flight controller (detailed in the Supplementary Materials) can be regarded as two parallel control loops consisting of altitude and lateral position controllers. The flight altitude is regulated by the total thrust generated from the two wings, quadratic to the yaw rate as established in Eq. 6. The desired yaw rate is realized through the yaw torque produced by the sum of the propelling thrusts $t_{p,1} + t_{p,2}$ as governed by Eq. 5. This allows us to manipulate the closed-loop attitude dynamics to ensure that the robot stays aloft at the desired height.

Unlike multirotor (*69*–*71*) or flapping-wing (*1*, *20*, *13*, *12*, *72*–*75*) vehicles, which generate flight forces strictly along the vertical body axis and must moderate the attitude to induce lateral acceleration, the proposed robot is capable of producing horizontal forces while remaining approximately upright as the propelling thrusts are aligned with $\hat{\mathbf{y}}$ as $(t_{p,1} - t_{p,2})\hat{\mathbf{y}}$ (Figs. 1B and 3A), whereas the direction of the $\hat{\mathbf{y}}$ axis ($\hat{\mathbf{y}} = [-\sin\psi, \cos\psi]^T$) swiftly rotates at the rate Ω_z (Eq. 7). However, the direct attempt to use this characteristic for controlling the horizontal position can destabilize the flight attitude because the term is also present in the reduced attitude dynamics (Eq. 9). Hence, the lateral position controller must stabilize both the position and attitude of the robot simultaneously, including taking into account and compensating for the gyroscopic terms (see the Supplementary Materials). Furthermore, the devised strategy addresses the challenge associated with the underactuation of the two-rotor vehicle. The developed controller computes the desired horizontal force vector $\mathbf{f}$ defined in the inertial frame, and the differential thrust commanded to the robot is proportional to the projection of $\mathbf{f}$ along the thrust direction $\hat{\mathbf{y}}$ or $t_{p,1} - t_{p,2} = 2\hat{\mathbf{y}}^T\mathbf{f}$. Over one cycle of yaw rotation, the vector sum of the propeller thrust averages to $\mathbf{f}$ (see the Supplementary Materials). That is, the lateral position control is achieved with only one degree of freedom input: $t_{p,1} - t_{p,2}$ on the cycle averaged basis. Overall, the proposed technique permits the 3D translational dynamics of the robot equipped with only two actuators to be controlled for a trajectory-tracking flight. The cycle-average approach, nevertheless, implies that the bandwidth of the control input is restricted and determined by the revolving rate. This may prevent the robot from tracking the desired trajectories as accurately as conventional rotorcraft.

With the fabricated prototype and developed control framework, flight experiments were first conducted to verify the stability property (the flight environment and setup are detailed in Materials and Methods). Initially, the center of mass of the prototype was manually tuned to achieve robust attitude stability. To assess its passive stability, the robot was suspended at a height of 2 m by a programmed gripper. Immediately after the release, the motors were powered with only the altitude controller enabled to maintain an approximately constant height. Thereafter, the robot remained upright for over 50 s before leaving the flight arena (movie S1), attesting the predicted passive stability. To illustrate that there exists a region of l_{cp} that satisfies the stability conditions predicted by Eq. 13, we shifted the battery (8.00 g) downward and upward from the original position by 4.2 and 0.9 cm, respectively. The relocations slightly increased and decreased the value of l_{cp}. The robot still demonstrated inherent stability (movie S1).

The experiments were repeated after the battery was displaced downward further to 6.2 cm from the original configuration. In this scenario, the robot crashed within 3 s after it was released (movie S1). As captured by Eq. 13, the increase in the inertia I_d is likely the cause of the observed instability. Similarly, the attempt to reduce l_{cp} by displacing the battery upward from the original arrangement by 1.8 cm yielded an unstable flight as anticipated. The robot crashed within 5 s after it was released (movie S1).

To quantify the robot's attitude during these test flights, the angle between the robot's $\hat{\mathbf{z}}$ axis and the vertical axis (ϕ in Fig. 3A) is visualized to reflect the attitude stability of the vehicle. For the well-tuned prototype and the other two stable scenarios, it can be seen that ϕ slightly oscillated over time but mostly remained under 20° for the entire flight period (Fig. 3B). The trajectory plot of the well-tuned prototype manifests that it stayed within the small volume of 2 m by 2 m by 2 m (Fig. 3C). In contrast, the attitude of the robot with a notably displaced battery (downward by 6.2 cm and upward by 1.8 cm) swiftly diverged in less than 5 s (Fig. 3D). The outcomes corroborate that having the center of mass below the center of pressure is not a sufficient condition for attitude stability.

Furthermore, we demonstrated that the inherent stability is insensitive to fabrication precision. This was carried out by enlarging one of the wings by about 7.5% at the wing tip (fig. S6, A and B), creating an asymmetry configuration. In the flight test, the modified robot still achieved a stable uncontrolled flight (fig. S6C and movie S1).

Next, a position-controlled flight was performed using the developed control strategy. A smooth trajectory consisting of three characteristic motions (hovering, horizontal, and vertical translations) was chosen. Despite the presence of the slight tracking delay likely caused by the cycle-average control strategy, the robot successfully stabilized its position against the prescribed reference for the entire flight (Fig. 3, E and F, and movie S2). The result illustrates the effectiveness of the devised position controller and the trajectory-tracking capability of the vehicle.

Flight endurance and power expenditure

The power efficiency of a MAV can be evaluated from its power consumption and flight endurance (because the practical capacity of a battery is substantially affected by the discharge rate owing to the internal resistance). Power consumption is a relatively direct metric for efficiency, whereas flight time is more relevant to real-world applications. Both aspects are investigated for the proposed bioinspired flight platform.

The following assessment aims to benchmark both endurance and power consumption of the revolving-wing robot against its hardware baselines. We selected a widely used multirotor vehicle (Bitcraze, Crazyflie 2.1, 32.1 g with retroreflective markers) as the first reference vehicle and constructed a benchmark quadcopter from the same principal components as the proposed robot (avionics, motors, and propellers, totaling 39.2 g) as the second reference robot. To characterize the endurance, we performed extended hovering flights, during which the battery voltages were logged, with the aforementioned robots. The open-circuit voltage of a single-cell 250-mAh Li-Ion battery used in these robots is 4.2 V. As soon as the flight started, the voltage immediately dropped owing to the discharging current (fig. S7) and continued to decline over time. We commanded the robots to hover until the batteries were exhausted such that they were no longer able to stay aloft and recorded their total flight times (Fig. 5, fig. S7, and movie S3). The endurance of the proposed revolving vehicle was 894 s or 14.9 min, over twice as long as the reference robots (380 and 241 s; table S1) despite being similar in weight and components. To further enhance the flight time of the revolving-wing drone, the 250-mAh battery was substituted with a 650-mAh cell (15.7 g). This resulted in an overall mass of 42.8 g. The revolving-wing robot with an extended battery capacity was able to hover for 1470 s or 24.5 min (Fig. 5, fig. S7, and movie S3). This substantial improvement was obtained despite the fact that the increase in mass implies that the robot was no longer operating at its optimal condition.

The lack of onboard current sensors prevents directly recording the power consumption of the robots during flight. Instead, the power of the revolving-wing robot was evaluated by a benchtop hardware-in-the-loop (HIL) experiment (detailed in Materials and Methods). To replicate the flight condition experienced by the robot, the vehicle, together with a customized current and voltage measurement module (with a separate power supply), was mounted on the revolving platform driven by a servomotor (fig. S8A). During the test, we applied the average of the motor voltages recorded during the 894-s hovering flight to drive the motors and propellers and simultaneously commanded the servo motor to rotate at the speed identical to the robot's averaged revolving speed during the flight. The discharge current

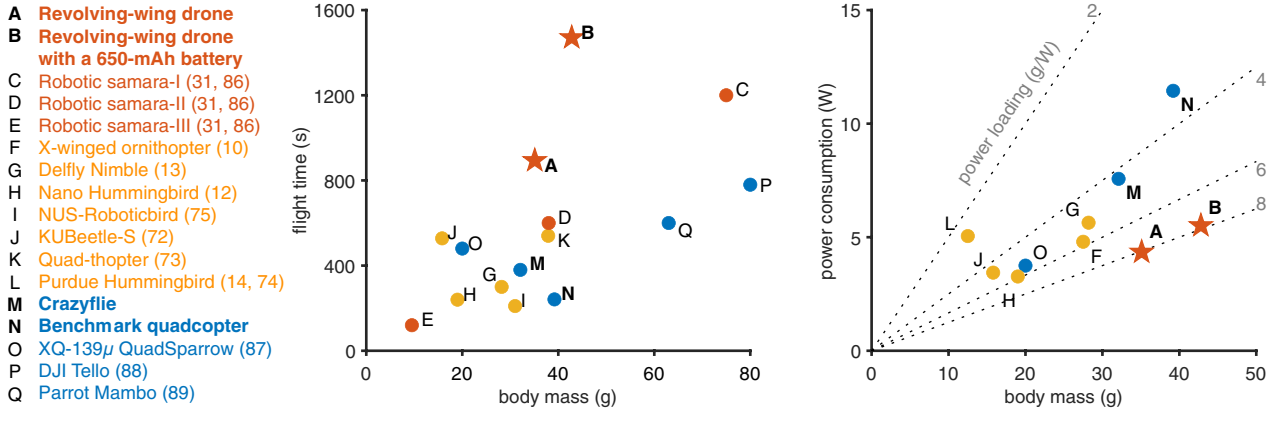

Fig. 5. Flight time, power consumption, and power loading of lightweight (less than 100 g) hovering-capable MAVs. Examples include three drone types: samara-like (orange), flapping-wing (yellow), and rotary-wing (blue) (refer to table S1 for detailed data).

from the battery and its voltage were logged to evaluate the power dissipated by the entire robot platform (including both the avionics and the actuators). During the test, the total vertical thrust produced by the robot was found to be equal to its weight and the torque summed to zero as anticipated (fig. S8B). This verifies that the condition resembled an actual hovering flight. From three repeated 30-s trials, the average power consumption was found to be 4.39 ± 0.12 W. In comparison, the power consumption of a Crazyflie and the benchmark quadcopter were also evaluated in another HIL setup (detailed in Materials and Methods). They were found to be 7.57 ± 0.06 W and 11.4 ± 0.4 W, both markedly higher than that of the revolving-wing robot (Fig. 5) and in accordance with the recorded flight times.

To compare the efficiency of the developed vehicle with other lightweight hovering-capable platforms, taking into account the scaling or size effects (*7*), we calculated the power loading of the revolving-wing drone, reference robots, and other established platforms that weigh under 100 g. The power loading of the developed prototype is as high as 8.0 g/W and approximately twice as large as those of the reference multirotor robots (4.2 g/W and 3.4 g/W; Fig. 5 and table S1). This is primarily attributed to the use of large revolving wings (as opposed to small propellers) as the main lift generation mechanism. The improved aerodynamic efficiency is a consequence of the low disk loading (recall that for aerodynamic power, $PL \propto DL^{-1/2}$). In relation to other lightweight robots, the revolving-wing robot demonstrates superior power loading (even when compared with flapping-wing vehicles with relatively low disk loading), with the flight time considerably longer than vehicles that are twice as heavy (Fig. 5 and table S1). The outcomes thoroughly highlight the benefits of the optimized revolving-wing mechanism.

DISCUSSION

In this work, we took motivation from autorotating plant seeds and developed a highly efficient revolving-wing robot. Two key flight mechanisms of maple seeds, namely, elevated lift generated from a prominent LEV and the stable gyration, are replicated by the propeller-driven robot. On the basis of studies on unsteady aerodynamics from low aspect ratio flapping and spinning wings, we collaborated the idea that quasi-steady models are suitable for the development of a centimeter-scale revolving-wing robot, allowing the interplay between aerodynamic forces and flight energetics to be accurately predicted. Through the use of parametric designs and empirically determined force coefficients, the wing profiles, when paired with the selected propulsion mechanism, were synergically optimized for the overall flight efficiency. The outcomes display several characteristics distinctive from biomimetic designs, reflecting the different requirements for powered gyrating and autorotating flights. Despite the dissimilarity, the use of sizable revolving wings for powered flight at this scale brings about a substantial reduction in energy consumption. As verified through a series of flight experiments, the bioinspired platform, with the extremely low disk loading of 1.2 N/m^2 [approximately one to two orders of magnitude smaller than that of flapping-wing robots and multirotor vehicles of similar size (*45*, *9*)], demonstrated over a twofold increase in overall power loading when compared with multirotor robots of similar weights. As a consequence, the 42.8-g prototype was able to stay airborne for 24.5 min.

The samara-inspired platform presented here may ultimately lead to hovering-capable aerial vehicles with enhanced efficiency, alleviating the severely restrictive flight times of small drones when it comes to practical applications (*7*, *8*). However, the introduction of spinning wings and resultant aerodynamics comes with associated increased complexity in flight dynamics. Thus far, our analysis is limited to rigid, flat, uncambered wings to facilitate the vehicular design and optimization process. It is foreseeable that the flight performance is likely to benefit from wings with more elaborate cambered profiles, twisted blades, or flexibility (*76*). To comprehensively capture the unsteady aerodynamics in such cases, the use of high-fidelity models or computational fluid dynamics is likely preferred.

Alternative to the goal of optimized flight endurance, a different objective function could be used to search for the configuration with, for instance, maximized payload capacity (*44*). The ability to morph aerodynamic surfaces for different operating conditions or flight envelopes as realized in (*77*, *58*, *78*, *57*) would further extend the flight capabilities. This could potentially be concurrently integrated with the biohybrid approach by fabricating morphing wings from real bird features (*58*). The study on wing efficacy performed on 26 spinning wings from 12 hummingbird taxa reports the power factor of almost 7.0 when the angle of attack is 16° (*15*), notably higher than 5.1 obtained with the optimized flat wings in this work. Nonetheless, for optimal vehicle performance, the efficiency of the propulsion mechanism must be taken into account as conducted in this study.

System-level power analysis

The framework developed to construct a highly efficient flyer in this work has been presented from the bottom-up approach, citing the low disk loading of the robot as the primary basis behind the superior flight efficiency. To gain further insights, we provide a systemic analysis to pinpoint the fundamental reasons behind the illustrated performance. Here, we demonstrate how the optimized configuration of the vehicle with large revolving wings actuated by two small motor-driven propellers leads to the high power loading illustrated by the vehicle.

Apart from the power loading of the vehicle *PL*, another quantity of interest is the dimensionless figure of merit $\eta < 1$, which captures the ratio of the actualized aerodynamic power to the mechanical input power of an actuator disk. The figure of merit quantifies directly the aerodynamic efficiency, brushing aside the impact of the actuation efficiency. Because η is dimensionless, its value is relatively scale independent [$0.3 < \eta < 0.8$ (*9*, *56*)], in contrast to both *PL* and *DL*.

In the context of the revolving-wing drone, the revolving wings and motor-driven propellers can be regarded as two cascaded actuator disks. The figure of merit of the vehicle is defined to be the aerodynamic power of the rotating wings over the mechanical input power of the propellers. Taking into account the free-stream air perceived by the propellers, it turns out that the figure of merit of the robot η_r is determined by the product of those of the two actuator disks according to (see the Supplementary Materials for the derivation)

$$\eta_r = \sigma \eta_w \eta_p \tag{14}$$

where the subscripts w and p refer to the wing and propeller subsystems and $\sigma \in [0,1]$ is a factor dependent on the ratio of the induced velocity of the propeller to its perceived free-stream flow $v_i/\Omega r_m$. In the optimized vehicle, it is anticipated that $\sigma \approx 1$ (see the

Supplementary Materials). Because $\eta_p, \eta_r < 1$, the outcome reveals a marked reduction in the overall aerodynamic efficiency caused by staging the two propulsion mechanisms together.

Nonetheless, unlike the power loading, the figure of merit alone does not directly predict the magnitude of the thrust or comprehend the scaling effects. To make the connection, we use the fact that the figure of merit can be written in terms of mechanical power loading PL_m (thrust over mechanical input power) and disk loading: $\eta = PL_m \cdot \sqrt{DL}/\sqrt{2\rho}$ (*9*). Because the disk loading of the vehicle and the revolving wings are identical, the result from Eq. 14 develops into

$$PL_{m,r} \approx \eta_p PL_{m,w} \tag{15}$$

That is, the mechanical power loading of the robot is lower than that of the wings. Because PL_m scales with the disk loading as $PL_m \propto DL^{-1/2}$ (*9*), the mechanical power loading of the vehicle and the wings is notably higher than that of its main propulsion mechanism or the propellers because of the difference in the disk areas. It is estimated that, in the flight conditions, $\eta_p \approx 1/3$ and $PL_{m,w} \approx 6PL_{m,p}$. As a consequence, $PL_{m,r} \approx 2PL_{m,p}$ (see the Supplementary Materials). That is, the inclusion of sizable revolving wings roughly doubles the power loading of the vehicle when compared with multirotor platforms that are directly driven by small propellers. The conclusion is consistent with the reported power measurements (Fig. 5 and table S1), which verifies that the power loading of the revolving drone is twice as high as that of the benchmark quadcopter manufactured from the same propulsion components.

Advantages of the revolving motion on potential applications

Despite the associated complexity in modeling and the requirement to continuously rotate, the advantages brought by the revolving wings extend beyond their influence on flight energetics. In flight, additional aerodynamic forces and the continuous rotation affect the attitude stability. The wings take a role akin to aerodynamic dampers that enable the robot to passively stabilize its attitude to upright even in the absence of fast attitude feedback. This is dissimilar to most small hovering-capable robots (*60*, *13*, *14*, *68*), as it is suggested that a mechanism for passive stabilization may only be present in some hawk moths and hummingbirds (*79*). The revolving motion also benefits the maneuverability, allowing the position of the robot to be controlled despite having only two actuators.

In addition, we provide examples that the fast rotation offers certain advantages when it comes to sensing and localization when paired with suitable sensors, such as a laser ranger (*80*) or a camera (*81*). First, we demonstrate how a laser ranger can be used on the revolving-wing drone. A multiranger module [Bitcraze, Multi-ranger deck (*82*)], containing directional tiny time-of-flight sensors (3.0 g), was incorporated into the robot (fig. S9). Each sensor is capable of detecting an obstacle up to 4 m. Leveraging the revolving motion of the robot in hover, the map of the robot's environment was constructed using the data from two horizontally directed sensors measured at 10 Hz during an 18-s flight (see Fig. 6 for the result and the Supplementary Materials for the implementation details). The inherent rotation assists the robot to scan the surroundings in a similar manner to a conventional light detection and ranging (LiDAR) instrument, but without the need for a rotating mirror. In the second example, a monochrome camera with 75° field of view was incorporated to construct panoramic videos, exploiting the revolving motion. In this experiment, a complementary metal-oxide semiconductor (CMOS) camera and its controller (Arducam OV9281 and Raspberry Pi Zero W, totalling 21.5 g or 60% of the original vehicle's weight) were mounted on the robot (fig. S10). In the 36-s flight without lateral position control, the camera was triggered to take photos every 90° of rotation (about 14 frames per second for a revolving rate of 22 rad/s). Four videos (≈3.5 frames per second) were reconstructed, with each video capturing one direction (refer to Fig. 6C and movie S5). The outcomes not only illustrate the ability of the robot to broadly observe the environments but also manifest the high payload capability of the vehicle.

Comparison with tip-jet helicopters

The principle of using thrust devices to drive rotating blades for flight adopted by the proposed samara-inspired drone was previously used in human-scale tip-jet rotorcraft (*40*–*43*). With central jet engines and nozzles installed at the blade tips for propelling the rotor blades, tip-jet helicopters differ from conventional helicopters because they eliminate anti-torque devices or a tail rotor. It can be seen that motor-driven propellers on the revolving-wing drone play an equivalent role to the jet propulsion.

For tip-jet helicopters, the efficiency is majorly influenced by the propulsion efficiency. This is theoretically optimized when the tip translational velocity is half of the jet exhaust velocity (*41*, *42*). Therefore, it is preferred to obtain a high blade tip speed to match the inherently exceedingly fast jet exhaust velocity. This subsequently demands rotors with large radii and aspect ratios. The requirements for efficiency inevitably conflict with the structural constraints, resulting in vehicles with subpar flight efficiency.

As elucidated by this study, the efficiency of the propulsion of the revolving-wing drone is similarly dependent on the translational air speed perceived by the motor-driven propellers, referred to as the free-stream velocity $v_s = \Omega r_m$ as evidenced in Fig. 2G. The use of motor-driven propellers and low aspect ratio wings at this scale, on the other hand, does not lead to the mismatch present in human-scale tip-jet rotorcraft. As a result, a highly efficient flyer can be engineered through the devised optimization strategy.

Furthermore, other notable drawbacks such as noise from the jet engine or complications related to the transmission of hot compressed air through the blades are absent from the centimeter-scale revolving-wing drone. This renders the configuration more attractive for MAVs.

MATERIALS AND METHODS

Aerodynamic model of the revolving wings

The primary function of the aerodynamic model for the revolving wings is to predict C_T and C_Q according to its wing shape parameters and the wing pitch angle. BEM and MT are used.

The elemental lift and drag in Eq. 2 are perpendicular to and parallel with the relative air velocity vector $V(r)$, as illustrated in fig. S1. The local geometric angle of attack $[\alpha(r)]$ is defined as the angle between the incoming air and the wing chord. Provided that the wing pitch angle is β, the elemental forces from the wing pair contribute to the thrust and drag torque through the following projection:

$$dT = 2(dF_L \cos(\beta - \alpha) - dF_D \sin(\beta - \alpha)) \tag{16}$$

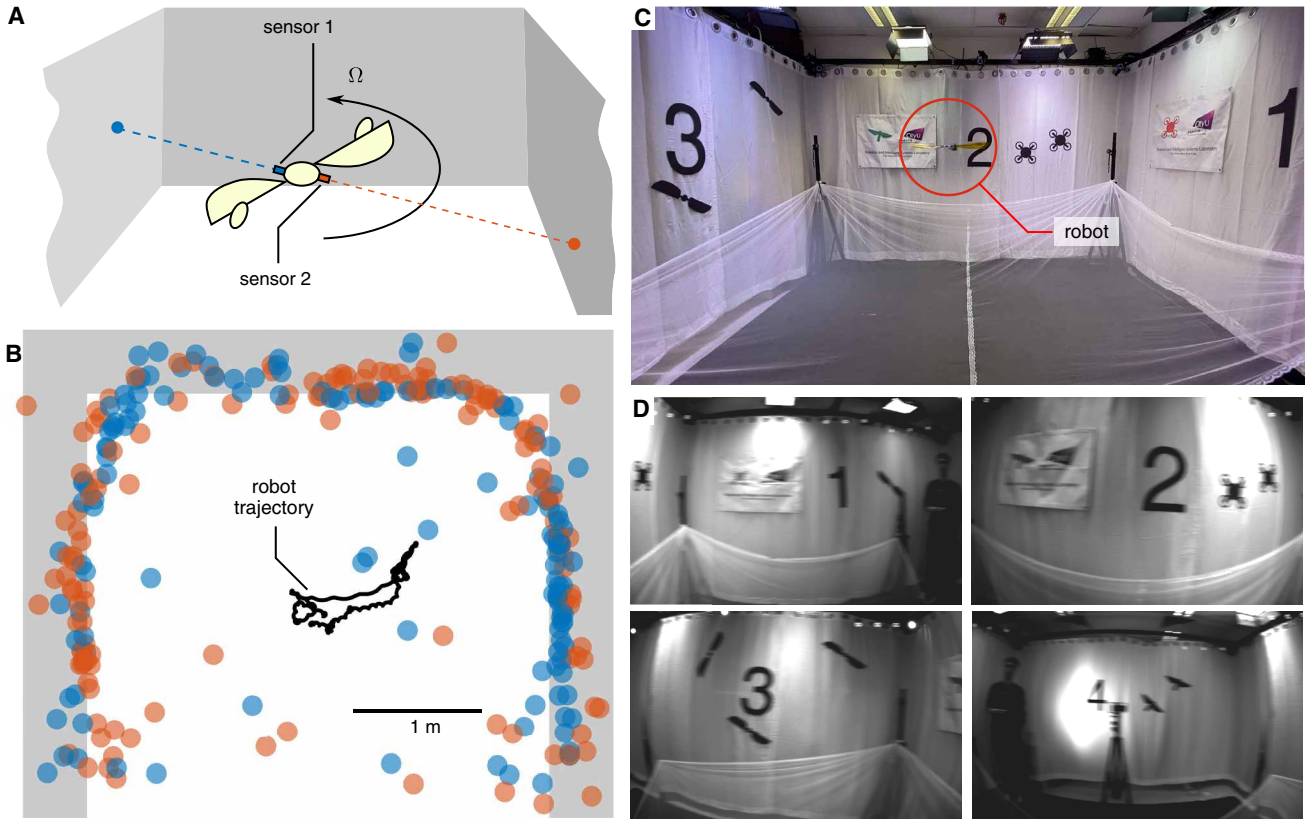

Fig. 6. Demonstrations of potential applications related to vision and perception benefiting from the revolving motion of the vehicle. (**A**) Schematic diagram illustrating the mapping (distance measurement) method using two time-of-flight sensors. (**B**) Result of the reconstructed map from the 18-s flight of the robot carrying the time-of-flight sensors. (**C**) Image of the the four-walled flight environment for the video recording. (**D**) Four consecutive photos captured by the on-board camera. The images shown were taken within one rotation cycle (≈280 ms) during the 36-s flight.

$$\mathrm{d}Q = 2r(\mathrm{d}F_{\mathrm{L}}\sin(\beta-\alpha) - \mathrm{d}F_{\mathrm{D}}\cos(\beta-\alpha)) \tag{17}$$

In addition to BEM, the general MT is applied to predict elemental thrust and torque by regarding the revolving wings and an infinitesimally actuator disk with the assumptions that the air is homogeneous and inviscid, and the flow is steady, axisymmetric, and incompressible. MT presumes a pressure discontinuity along the streamtube over the actuator disk, attributing to the induced velocity at the rotor. In the presence of the wake rotation, the induced velocity consists of axial (V_{a}) and tangential (V_{t}) components (fig. S1). The conservation of linear and angular momentum applied to an annular streamtube dr at radial distance r yields (*50*)

$$\mathrm{d}T(r) = 4\pi r\rho\gamma(r)\,V_{\mathrm{a}}^2(r)\,\mathrm{d}r \tag{18}$$

$$\mathrm{d}Q(r) = 4\pi r^2\rho\gamma(r)\,V_{\mathrm{a}}(r)\,V_{\mathrm{t}}(r)\,\mathrm{d}r \tag{19}$$

where the free-stream velocity is neglected for a hovering vehicle, and

$$\gamma(r) = \frac{2}{\pi}\arccos(e^{-\epsilon(r)}) \text{ with } \epsilon(r) = \frac{r_{\mathrm{tip}} - r}{r\sin(\beta-\alpha)} \tag{20}$$

is a correction factor for the tip loss ($\gamma \le 1$) that empirically models the reduced blade forces in the vicinity of the wing tips ($r \to r_{\mathrm{tip}}$) (*51*). Unlike 1D MT, the inclusion of the rotational wake in the model enables the drag torque to be predicted without using an empirically determined induced power factor.

To consolidate the results from BEM and MT, the incoming airspeed at a wing element is computed from the sum of the induced velocity and the blade rotation: $V^2 = (r\Omega - V_{\mathrm{t}}(r))^2 + V_{\mathrm{a}}^2(r)$ with the associated angle of attack $\alpha(r) = \beta - \arctan(V_{\mathrm{a}}/V_{\mathrm{t}} - \Omega r)$ as illustrated in fig. S1. Equating Eqs. 17 to 19 eliminates the dependency on V, V_{a}, V_{t}, and α, allowing the thrust and torque coefficients to be evaluated by integrating the blade elements from the rotation axis to the wing tip

$$C_T = \frac{1}{\Omega^2}\int_{r=0}^{r_{\mathrm{tip}}}\mathrm{d}T,\; C_Q = \frac{1}{\Omega^2}\int_{r=0}^{r_{\mathrm{tip}}}\mathrm{d}Q$$

As a result, C_T and C_Q are only dependent on the wing chord profile $c_{\mathrm{h}}(r)$, the blade pitch angle β, and lift and drag coefficients $C_{\mathrm{L/D}}(\alpha)$.

Experimental identification of the wing model

Six pairs of wings in Fig. 2A (no. 1 to 6) were fabricated from carbon fiber rods and 75-m polyimide film (Dupont Kapton). The designs with wide and sharp tips (no. 1 and 2) were included to reflect the modeled tip loss. Polyimide film was laser cut to the desired profiles using CO_2 laser (Epilog Mini 24) and attached to 1.8-mm-diameter

carbon fiber rods near the leading edges. Additional structural support was provided by 1.2-mm-diameter carbon fiber rods acting as wing ribs.

The experimental platform shown in Fig. 2B consists of a servo motor and a six-axis force and torque load cell (ATI, Nano 25). Using the encoder of the servo motor, the revolving speed of the wings was directly measured and controlled with a proportional-integral controller. The motor shaft was attached to a wing mount and a pair of wings to be tested. The horizontal offset between the motor and the load cell (150 mm) acted as a moment arm such that the thrust was measured by the sensor as torque along one of the horizontal axes. The drag torque was directly sensed along the vertical axis of the transducer.

For identification experiments, each wing pair was mounted on the setup at four or five wing pitch angles (between 0° and 50°), totaling 29 wing configurations. For each configuration, we measured the thrust and torque of the revolving wings at four to six rotational rates distributed between 2π and 14π rad/s. At each speed, three repeated measurements were carried out. Some data points at extreme rotational rates with observable wing deformation were excluded from the analysis (see the Supplementary Materials). One data point represents an average from a 20-s measurement taken at 200 Hz after the spinning rate had reached a steady state. A total of 12 to 18 data points were used to empirically determine the thrust and torque coefficients of each wing configuration by linear regression (fig. S2). Thereafter, 29 pairs of empirical thrust and torque coefficients were used for a nonlinear regression to evaluate a single set of force coefficients. We applied the Nelder-Mead simplex algorithm to obtain $\{C_{L0}, C_{L1}, C_{D0}, C_{D1}\}$ that minimizes the normalized prediction errors of C_T and C_Q described by the objective function

$$\arg\min_{C_{L0},C_{L1},C_{D0},C_{D1}} \sum_{i=1}^{29} \left(\frac{\widehat{C}_T - C_T}{C_T}\right)^2 + \left(\frac{\widehat{C}_Q - C_Q}{C_Q}\right)^2 \quad (21)$$

where $\widehat{C}_{T/Q}$'s represent predicted coefficients, $C_{T/Q}$'s are empirical coefficients, and $C_{T/Q}$'s are empirical coefficients averaged over 29 wing configurations.

Figure 2C compares the fitted and empirical coefficients. Within the given configurations of wing, the RMSEs of the C_T and C_Q predictions are 3.8×10^{-5} and 7.6×10^{-6} N · m · s^2/rad^2.

Propeller and DC motor models

The propeller's thrust and drag torque depend not only on its spinning speed ω but also on its axial translational velocity, equivalent to the free-stream velocity in the axial direction $v_s = r_m\Omega$. For conventional rotorcraft in hovering conditions, this velocity is often negligible. In the proposed vehicle, the propellers undergo notable translational speed originated by the vehicle's yaw rotation. Hence, the contributions from v_s cannot be ignored.

Unlike flat wings with known parameterized profiles, conventional rotor blades have varying degrees of blade pitch and thickness. A strategy used in the blade element analysis of the flat revolving wings is no longer suitable due to the complexity of the blade profile. For these reasons, a lumped model developed in (*56*) was used. The model assumes (i) a near-ideal pitch and chord variation around the hub and (ii) that the lift coefficient is linearly proportional to the angle of attack and the drag coefficient has a quadratic dependence on the lift coefficient. Although these assumptions may be violated to a certain degree, the model has demonstrated validity with propellers of similar scales (radius $r_p \approx 2$ cm) (*23*). The lumped parameter model provides the following expressions of thrust and torque after integrating over the entire blades

$$t_p = c_1\omega^2\left(c_2 - \frac{v_i + v_s}{r_p\omega}\right) \quad (22)$$

$$\tau_p = c_3\omega^2 + r_p t_p\left(\frac{\kappa_p v_i + v_s}{r_p\omega}\right) \quad (23)$$

where v_i is the induced velocity and c_i's are lumped coefficients. Simultaneously, MT states that

$$t_p = 4\pi r_p^2 \rho\, v_i(v_i + v_s) \quad (24)$$

Equalizing Eqs. 22 with 24 produces

$$v_i = \frac{1}{2}\sqrt{\left(\frac{c_1}{4\pi\rho} + \frac{v_s}{r_p\omega}\right)^2 + \frac{c_1}{\pi\rho}\left(c_2 - \frac{v_s}{r_p\omega}\right)} - \frac{1}{2}\left(\frac{c_1}{4\pi\rho} + \frac{v_s}{r_p\omega}\right) \quad (25)$$

Substituting the result back into Eqs. 22 and 23 yields the thrust and torque coefficients, which are dependent on $v_s/(r_p\omega)$ and other unknown constants (κ_p, c_1, c_2, c_3).

To relate the propeller's torque to the motor's driving voltage, a first-order model for brushed DC motors is used. The assumed steady-state conditions imply that the current and angular speed are constant, rendering the induced voltage and inertial terms insignificant. Suppose all constant parameters are determined, equating the motor torque $\tau_p = (u_m - k_m\omega)k_m/R_m$ with Eq. 23 using v_i from Eq. 25 enables us to numerically compute ω from u_m and v_s. In the end, this replaces the dependence of ω in $t_p = c_T\omega^2$ such that $t_p = f_p(u_m, v_s)$.

Motor parameter identification

The developed revolving-wing robot is equipped with two 7 mm–by–20 mm coreless motors (rated speed of 49,000 rounds/min at 3.7 V). To identify the relevant parameters, we exploit an alternative relation, $\tau_p = k_m i$ when i is the current, which leads to $u_m = iR_m + k_m\omega$. This allows R_m and k_m to be empirically determined from measurements of the driving voltage, current, and rotational speed.

A benchtop power supply (GW Instek GPD-3303S) was used to generate different driving voltages. The voltage and current (through a current sensor, GHS 10-SME, LEM Inc.) measurements were recorded through a data acquisition device (DAQ) (PCI-6229, National Instruments). The motor was driven when affixed with a propeller. Three types of propellers (fig. S11A), including a 40-mm four-blade propeller used in the robot prototype and two larger propellers, were selected for the identification to ensure that the experimental data cover a sufficiently large range of i and ω to confidently deduce the values of R_m and k_m. A noncontact tachometer (UNI-T, UT372) was installed on the setup for rotational speed measurements. For each propeller, the motor was supplied with five voltages from 0.1 to 3.0 V at the increment of ~0.5 V, resulting in the variations in the current and angular rate up to 1.8 A and 2025 rad/s. The linearly regressed result (fig. S11B) confirms that the dataset from three propellers adequately spans over the 2D fitted plane (the RMSE of the predicted ω is 25 rad/s; the residual errors of ω are shown in fig. S11C), allowing R_m and k_m to be confidently estimated as $R_m = 0.87 \pm 0.01$ Ω and $k_m = (6.58 \pm 0.07) \times 10^{-4}$ Vs/rad.

Propeller lumped model identification

The experimental platform used for testing the wing aerodynamics (Fig. 2B) was adapted for the identification of the actuator's model. Two motor-driven propellers were oppositely attached to the propeller mount residing on the shaft of the servo motor. Drive electronics (Arduino MKR1000, motor drivers, and batteries) were installed inside the propeller mount to allow the entire part to rotate. The load cell measured the thrust generated by the two propellers, amplified by the moment arm, through the torque about the vertical axis.

To eliminate aerodynamic drag contributed by the spinning structure, before the actual experiments, we separately measured the torqued caused by the rotating platform without driving the propellers at 11 free-stream velocities up to over 10 m/s. The drag torque was assumed a quadratic function of Ω. The measurements were used to compute the corresponding proportional constant. The obtained drag model was used for subtraction of measured torque.

Measurements for the identification of the propeller's coefficients (c_1, c_2, c_3, and κ_p) were first acquired when the propellers were at rest at seven voltages (12 data points in Fig. 2E). Then, at $u_m = 1.94$ V, the torque measurements were taken when the platform rotated at 12 different speeds (v_s varied from 0 to over 11 m/s). We recorded three measurements at each speed. The experiment was repeated with $u_m = 2.75$ V. All data were consolidated to estimate for propeller's coefficients by minimizing the squared errors between the thrust measurements and the predictions from the derived nonlinear model $f_p(u_m, v_s)$ using the Nelder-Mead simplex algorithm. Without current measurements from the motorized platform, the current and hence electrical input power can be estimated from the input voltage and measured thrust using the developed model and identified model parameters.

Vehicle profile and optimization constraints

In the flight endurance optimization, the wing profile was parameterized with the locations of wing root r_{root} and wing tip r_{tip}, and six-degree polynomial chord functions $c_h(r) = \sum_{i=0}^{i=6} \gamma_i r^i$. That is

$$\Theta = \{r_m, \beta, r_{root}, r_{tip}, \gamma_0, \ldots, \gamma_6\} \quad (26)$$

The maximum platform size was constrained by imposing r_m, $r_{tip} \leq 30$ cm. The constraint on the wing aspect ratio was translated into two parts. The first provides a lower bound for the desired aspect ratio $AR = (r_{tip} - r_{root})^2 / \int c_h(r) dr \geq 3.5$. The second part limits the maximum chord length according to $\max_r \ c_h(r) \leq (r_{tip} - r_{root})/3$. This is to discourage solutions with severely uneven area distribution. Overall, it is desirable to obtain wings with sufficiently low Rossby numbers (equivalent to the aspect ratio for a revolving wing) so that LEV remains stable (*55*, *49*).

Flight environment

Depending on the intention (open-loop or position-controlled flights), the control board (Bitcraze, Crazyflie 2.1) was programmed with customized flight controllers. Four reflective markers were mounted on the robot to obtain the pose feedback from the motion capture system (NaturalPoint, OptiTrack). In flight, a long-range radio (Bitcraze, CrazyRadio PA) was used for wireless communication with the ground station, transmitting the commands and logging the sensory data from the robot (see the Supplementary Materials for the implementation details).

Power and efficiency evaluation

In the benchtop HIL setup for the revolving-wing drone, the robot was mounted on the shaft of a servo motor of the rotating platform to simulate the revolving flight condition. A current and voltage measurement module with a separate power supply was installed on the robot to directly evaluate the power consumption of the robot as shown in fig. S8A. The module consisted of a single board computer (Arduino MKR WiFi 1010) that allowed the measured voltage and current during rotation to be logged via wireless communication at 30 Hz. To enhance the accuracy, an external 16-bit analog-to-digital converter (ADC) was used to read the battery voltage and output of the current sensor (ACS712) instead of the Arduino's built-in ADC. During the test, the effective motor voltage u_m (the product of the battery voltage and duty ratio) was controlled in real time via the prescribed motor commands.

In addition to the hovering revolving speed (18.8 rad/s), other revolving speeds were also tested to inspect the effect of the free-steam air on the power consumption of the motor-driven propellers. As predicted by the derived model of a motor-driven propeller, increasing the revolving speed lowered the power consumption (fig. S8B).

The evaluation of the power consumption of a Crazyflie and the benchmark quadcopter was carried out using a similar setup without a rotating platform. The voltage and current were directly logged using the DAQ (PCI-6229, National Instruments) through the current sensor (GHS 10-SME, LEM Inc.). The results of all power measurements are reported in table S1.

SUPPLEMENTARY MATERIALS

www.science.org/doi/10.1126/scirobotics.abg5913
Sections S1 to S7
Figs. S1 to S15
Table S1
Movies S1 to S5
References (*83*–*89*)

View/request a protocol for this paper from *Bio-protocol*.

REFERENCES AND NOTES

1. Y. Chen, H. Zhao, J. Mao, P. Chirarattananon, E. F. Helbling, N.-S. P. Hyun, D. R. Clarke, R. J. Wood, Controlled flight of a microrobot powered by soft artificial muscles. *Nature* **575**, 324–329 (2019).
2. V. Iyer, A. Najafi, J. James, S. Fuller, S. Gollakota, Wireless steerable vision for live insects and insect-scale robots. *Sci. Robot.* **5**, eabb0839 (2020).
3. D. Falanga, K. Kleber, D. Scaramuzza, Dynamic obstacle avoidance for quadrotors with event cameras. *Sci. Robot.* **5**, eaaz9712 (2020).
4. K. Shah, G. Ballard, A. Schmidt, M. Schwager, Multidrone aerial surveys of penguin colonies in antarctica. *Sci. Robot.* **5**, eabc3000 (2020).
5. A. Farinha, R. Zufferey, P. Zheng, S. F. Armanini, M. Kovac, Unmanned aerial sensor placement for cluttered environments. *IEEE Robot. Autom. Lett.* **5**, 6623–6630 (2020).
6. M. J. Anderson, J. G. Sullivan, T. K. Horiuchi, S. B. Fuller, T. L. Daniel, A bio-hybrid odor-guided autonomous palm-sized air vehicle. *Bioinspir. Biomim.* **16**, 026002 (2020).
7. D. Floreano, R. J. Wood, Science, technology and the future of small autonomous drones. *Nature* **521**, 460–466 (2015).
8. K. Karydis, V. Kumar, Energetics in robotic flight at small scales. *Interface Focus* **7**, 20160088 (2017).
9. M. Ramasamy, T. E. Lee, J. G. Leishman, Flowfield of a rotating-wing micro air vehicle. *J. Aircr.* **44**, 1236–1244 (2007).
10. Y.-W. Chin, J. M. Kok, Y.-Q. Zhu, W.-L. Chan, J. S. Chahl, B. C. Khoo, G. K. Lau, Efficient flapping wing drone arrests high speed flight using post-stall soaring. *Sci. Robot.* **5**, eaba2386 (2020).
11. S. P. Sane, The aerodynamics of insect flight. *J. Exp. Biol.* **206**, 4191–4208 (2003).
12. M. Keennon, K. Klingebiel, H. Won, Development of the nano hummingbird: A tailless flapping wing micro air vehicle, in *Proceedings of the 50th AIAA Aerospace Sciences Meeting Including the New Horizons Forum and Aerospace Exposition* (AIAA, 2012), p. 588.

13. M. Karásek, F. T. Muijres, C. De Wagter, B. D. Remes, G. C. de Croon, A tailless aerial robotic flapper reveals that flies use torque coupling in rapid banked turns. *Science* **361**, 1089–1094 (2018).
14. Z. Tu, F. Fei, J. Zhang, X. Deng, An at-scale tailless flapping-wing hummingbird robot. I. design, optimization, and experimental validation. *IEEE Trans. Robot.* **36**, 1511–1525 (2020).
15. J. W. Kruyt, E. M. Quicazán-Rubio, G. F. van Heijst, D. L. Altshuler, D. Lentink, Hummingbird wing efficacy depends on aspect ratio and compares with helicopter rotors. *J. R. Soc. Interface* **11**, 20140585 (2014).
16. U. Pesavento, Z. J. Wang, Flapping wing flight can save aerodynamic power compared to steady flight. *Phys. Rev. Lett.* **103**, 118102 (2009).
17. E. W. Hawkes, D. Lentink, Fruit fly scale robots can hover longer with flapping wings than with spinning wings. *J. R. Soc. Interface* **13**, 20160730 (2016).
18. G. D. Goh, S. Agarwala, G. L. Goh, V. Dikshit, S. L. Sing, W. Y. Yeong, Additive manufacturing in unmanned aerial vehicles (uavs): Challenges and potential. *Aerospace Sci. Technol.* **63**, 140–151 (2017).
19. H. Klippstein, A. D. D. C. Sanchez, H. Hassanin, Y. Zweiri, L. Seneviratne, Fused deposition modeling for unmanned aerial vehicles (uavs): A review. *Adv. Eng. Mater.* **20**, 1700552 (2018).
20. Y. Chen, H. Wang, E. F. Helbling, N. T. Jafferis, R. Zufferey, A. Ong, K. Ma, N. Gravish, P. Chirarattananon, M. Kovac, R. J. Wood, A biologically inspired, flapping-wing, hybrid aerial-aquatic microrobot. *Sci. Robot.* **2**, eaao5619 (2017).
21. M. Graule, P. Chirarattananon, S. B. Fuller, N. T. Jafferis, K. Y. Ma, M. Spenko, R. Kornbluh, R. J. Wood, Perching and takeoff of a robotic insect on overhangs using switchable electrostatic adhesion. *Science* **352**, 978–982 (2016).
22. K. Hang, L. Ximin, H. Song, J. A. Stork, A. M. Dollar, D. Kragic, F. Zhang, Perching and resting-a paradigm for uav maneuvering with modularized landing gears. *Sci. Robot.* **4**, eaau6637 (2019).
23. Y. H. Hsiao, P. Chirarattananon, Ceiling effects for hybrid aerial–surface locomotion of small rotorcraft. *IEEE/ASME Trans. Mechatronics* **24**, 2316–2327 (2019).
24. K. Y. Ma, P. Chirarattananon, S. B. Fuller, R. J. Wood, Controlled flight of a biologically inspired, insect-scale robot. *Science* **340**, 603–607 (2013).
25. S. B. Fuller, Four wings: An insect-sized aerial robot with steering ability and payload capacity for autonomy. *IEEE Robot. Autom. Lett.* **4**, 570–577 (2019).
26. R. Å. Norberg, Autorotation, self-stability, and structure of single-winged fruits and seeds (samaras) with comparative remarks on animal flight. *Biol. Rev.* **48**, 561–596 (1973).
27. K. Varshney, S. Chang, Z. J. Wang, The kinematics of falling maple seeds and the initial transition to a helical motion. *Nonlinearity* **25**, C1 (2011).
28. M. D. Pirie, B. B. Klitgaard, R. T. Pennington, Revision and biogeography of *Centrolobium* (Leguminosae - Papilionoideae). *Syst. Bot.* **34**, 345–359 (2009).
29. D. Lentink, W. B. Dickson, J. L. Van Leeuwen, M. H. Dickinson, Leading-edge vortices elevate lift of autorotating plant seeds. *Science* **324**, 1438–1440 (2009).
30. E. R. Ulrich, J. S. Humbert, D. J. Pines, Pitch and heave control of robotic samara micro air vehicles. *J. Aircr.* **47**, 1290–1299 (2010).
31. E. R. Ulrich, D. J. Pines, J. S. Humbert, From falling to flying: The path to powered flight of a robotic samara nano air vehicle. *Bioinspir. Biomim.* **5**, 045009 (2010).
32. S. Jameson, K. Fregene, M. Chang, N. Allen, H. Youngren, J. Scroggins, Lockheed Martin's samarai nano air vehicle: Challenges, research, and realization, in *Proceedings of the 50th AIAA Aerospace Sciences Meeting Including the New Horizons Forum and Aerospace Exposition* (AIAA, 2012), p. 584.
33. P. Pounds, S. Singh, Samara: Biologically inspired self-deploying sensor networks. *IEEE Potentials* **34**, 10–14 (2015).
34. J. E. Low, L. T. S. Win, D. S. B. Shaiful, C. H. Tan, G. S. Soh, S. Foong, Design and dynamic analysis of a transformable hovering rotorcraft (thor), in *Proceedings of the 2017 IEEE International Conference on Robotics and Automation (ICRA)* (IEEE, 2017), pp. 6389–6396.
35. J. E. Low, L. T. S. Win, J. Le Lee, G. S. Soh, S. Foong, Towards a stable three-mode transformable hovering rotorcraft (thor), in *Proceedings of the 2018 IEEE/ASME International Conference on Advanced Intelligent Mechatronics (AIM)* (IEEE, 2018), pp. 492–497.
36. J. E. Low, D. Sufiyan, L. S. T. Win, G. S. Soh, S. Foong, Design of a hybrid aerial robot with multi-mode structural efficiency and optimized mid-air transition. *Unmanned Syst.* **07**, 195–213 (2019).
37. S. K. H. Win, L. S. T. Win, D. Sufiyan, G. S. Soh, S. Foong, Dynamics and control of a collaborative and separating descent of samara autorotating wings. *IEEE Robot. Autom. Lett.* **4**, 3067–3074 (2019).
38. D. S. B. Shaiful, L. T. S. Win, J. E. Low, S. K. H. Win, G. S. Soh, S. Foong, Optimized transition path of a transformable hovering rotorcraft (thor), in *Proceedings of the 2018 IEEE/ASME International Conference on Advanced Intelligent Mechatronics (AIM)* (IEEE, 2018), pp. 460–465.
39. B. H. Kim, K. Li, J.-T. Kim, Y. Park, H. Jang, X. Wang, Z. Xie, S. M. Won, H.-J. Yoon, G. Lee, W. J. Jang, K. H. Lee, T. S. Chung, Y. H. Jung, S. Y. Heo, Y. Lee, J. Kim, T. Cai, Y. Kim, P. Prasopsukh, Y. Yu, X. Yu, R. Avila, H. Luan, H. Song, F. Zhu, Y. Zhao, L. Chen, S. H. Han, J. Kim, S. J. Oh, H. Lee, C. H. Lee, Y. Huang, L. P. Chamorro, Y. Zhang, J. A. Rogers, Three-dimensional electronic microfliers inspired by wind-dispersed seeds. *Nature* **597**, 503–510 (2021).
40. R. Miller, Jet propulsion applied to helicopter rotors. *J. Aeronaut. Sci.* **13**, 639–645 (1946).
41. J. Nichols, "Tip-mounted turbojets for helicopter propulsion—A progress report" (Technical Report, SAE Technical Paper, 1964).
42. J. Phillips, An efficient tip jet drive, in *Aircraft Design and Operations Meeting* (AIAA, 1991), p. 3124.
43. N. Kolarević, S. Crnojević, M. Stanković, N. Latković, M. Miloš, Experimental verification of performance of tip-jet helicopter propulsion system. *Mater. Today* **32**, 112–117 (2020).
44. S. Bai, P. Chirarattananon, Design and take-off flight of a samara-inspired revolving-wing robot, in *Proceedings of the 2019 IEEE/RSJ International Conference on Intelligent Robots and Systems (IROS)* (IEEE, 2019), pp. 6070–6076.
45. H. V. Phan, H. C. Park, Mimicking nature's flyers: A review of insect-inspired flying robots. *Curr. Opin. Insect Sci.* **42**, 70–75 (2020).
46. H. V. Phan, H. C. Park, Mechanisms of collision recovery in flying beetles and flapping-wing robots. *Science* **370**, 1214–1219 (2020).
47. S. P. Sane, M. H. Dickinson, The control of flight force by a flapping wing: Lift and drag production. *J. Exp. Biol.* **204**, 2607–2626 (2001).
48. Z. J. Wang, Aerodynamic efficiency of flapping flight: Analysis of a two-stroke model. *J. Exp. Biol.* **211**, 234–238 (2008).
49. Y. J. Lee, K. B. Lua, T. T. Lim, K. S. Yeo, A quasi-steady aerodynamic model for flapping flight with improved adaptability. *Bioinspir. Biomim.* **11**, 036005 (2016).
50. E. Branlard, *Wind Turbine Aerodynamics and Vorticity-Based Methods* (Springer, 2017), vol. 10.
51. D. H. Wood, V. L. Okulov, D. Bhattacharjee, Direct calculation of wind turbine tip loss. *Renew. Energy* **95**, 269–276 (2016).
52. O. Gur, A. Rosen, Propeller performance at low advance ratio. *J. Aircr.* **42**, 435–441 (2005).
53. J. Morgado, M. Silvestre, J. Páscoa, Validation of new formulations for propeller analysis. *J. Propulsion Power* **31**, 467–477 (2015).
54. K. Sum Wu, J. Nowak, K. S. Breuer, Scaling of the performance of insect-inspired passive-pitching flapping wings. *J. R. Soc. Interface* **16**, 20190609 (2019).
55. D. Lentink, M. H. Dickinson, Rotational accelerations stabilize leading edge vortices on revolving fly wings. *J. Exp. Biol.* **212**, 2705–2719 (2009).
56. M. Bangura, R. Mahony, Thrust control for multirotor aerial vehicles. *IEEE Trans. Robot.* **33**, 390–405 (2017).
57. E. Ajanic, M. Feroskhan, S. Mintchev, F. Noca, D. Floreano, Bioinspired wing and tail morphing extends drone flight capabilities. *Sci. Robot.* **5**, eabc2897 (2020).
58. E. Chang, L. Y. Matloff, A. K. Stowers, D. Lentink, Soft biohybrid morphing wings with feathers underactuated by wrist and finger motion. *Sci. Robot.* **5**, eaay1246 (2020).
59. M. W. Mueller, R. D'Andrea, Relaxed hover solutions for multicopters: Application to algorithmic redundancy and novel vehicles. *Int. J. Robot. Res.* **35**, 873–889 (2016).
60. N. T. Jafferis, E. F. Helbling, M. Karpelson, R. J. Wood, Untethered flight of an insect-sized flapping-wing microscale aerial vehicle. *Nature* **570**, 491–495 (2019).
61. M. Piccoli, M. Yim, Passive stability of vehicles without angular momentum including quadrotors and ornithopters, in *Proceedings of the 2015 IEEE International Conference on Robotics and Automation (ICRA)* (IEEE, 2015), pp. 1716–1721.
62. S. B. Fuller, Z. E. Teoh, P. Chirarattananon, N. O. Pérez-Arancibia, J. Greenberg, R. J. Wood, Stabilizing air dampers for hovering aerial robotics: Design, insect-scale flight tests, and scaling. *Auton. Robot.* **41**, 1555–1573 (2017).
63. D. Seter, A. Rosen, Stability of the vertical autorotation of a single-winged samara. *J. Appl. Mech.* **59**, 1000–1008 (1992).
64. V. M. Ortega-Jimenez, A. Martín-Alcántara, R. Fernandez-Feria, R. Dudley, On the autorotation of animal wings. *J. R. Soc. Interface* **14**, 20160870 (2017).
65. S. K. H. Win, L. S. T. Win, G. S. Soh, S. Foong, Design, modelling and control of collaborative samara autorotating wings (saw). *Int. J. Intell. Robot. Appl.* **3**, 144–157 (2019).
66. F. H. F. Handbook, U.S. Department of Transportation (2012); www.faa.gov.
67. M. Piccoli, M. Yim, Passive stability of a single actuator micro aerial vehicle, in *Proceedings of the 2014 IEEE International Conference on Robotics and Automation (ICRA)* (IEEE, 2014), pp. 5510–5515.
68. Bitcraze AB crazyflie 2.1; https://www.bitcraze.io/products/crazyflie-2-1/[accessed 21 August 2021].
69. D. Mellinger, N. Michael, V. Kumar, Trajectory generation and control for precise aggressive maneuvers with quadrotors. *Int. J. Robot. Res.* **31**, 664–674 (2012).
70. S. Bai, S. Tan, P. Chirarattananon, Splitflyer: A modular quadcoptor that disassembles into two flying robots, in *Proceedings of the 2020 IEEE/RSJ International Conference on Intelligent Robots and Systems (IROS)* (IEEE, 2020), pp. 1207–1214.
71. M. Faessler, A. Franchi, D. Scaramuzza, Differential flatness of quadrotor dynamics subject to rotor drag for accurate tracking of high-speed trajectories. *IEEE Robot. Autom. Lett.* **3**, 620 (2017).

72. H. V. Phan, S. Aurecianus, T. K. L. Au, T. Kang, H. C. Park, Towards the long-endurance flight of an insect-inspired, tailless, two-winged, flapping-wing flying robot. *IEEE Robot. Autom. Lett.* **5**, 5059–5066 (2020).
73. C. De Wagter, M. Karásek, G. de Croon, Quad-thopter: Tailless flapping wing robot with four pairs of wings. *Int. J. Micro Air Veh.* **10**, 244–253 (2018).
74. Z. Tu, F. Fei, L. Liu, Y. Zhou, X. Deng, Flying with damaged wings: The effect on flight capacity and bio-inspired coping strategies of a flapping wing robot. *IEEE Robot. Autom. Lett.* **6**, 2114–2121 (2021).
75. Q.-V. Nguyen, W. L. Chan, Development and flight performance of a biologically-inspired tailless flapping-wing micro air vehicle with wing stroke plane modulation. *Bioinspir. Biomim.* **14**, 016015 (2018).
76. L. Zhao, Q. Huang, X. Deng, S. P. Sane, Aerodynamic effects of flexibility in flapping wings. *J. R. Soc. Interface* **7**, 485–497 (2010).
77. A. Ramezani, S.-J. Chung, S. Hutchinson, A biomimetic robotic platform to study flight specializations of bats. *Sci. Robot.* **2**, eaal2505 (2017).
78. S.-M. Baek, S. Yim, S.-H. Chae, D.-Y. Lee, K.-J. Cho, Ladybird beetle–inspired compliant origami. *Sci. Robot.* **5**, aaz6262 (2020).
79. H. E. Taha, M. Kiani, T. L. Hedrick, J. S. Greeter, Vibrational control: A hidden stabilization mechanism in insect flight. *Sci. Robot.* **5**, eabb1502 (2020).
80. K. McGuire, C. De Wagter, K. Tuyls, H. Kappen, G. C. de Croon, Minimal navigation solution for a swarm of tiny flying robots to explore an unknown environment. *Sci. Robot.* **4**, eaaw9710 (2019).
81. S. Sun, G. Cioffi, C. De Visser, D. Scaramuzza, Autonomous quadrotor flight despite rotor failure with onboard vision sensors: Frames vs. events. *IEEE Robot. Autom. Lett.* **6**, 580 (2021).
82. Bitcraze AB multi-ranger deck; www.bitcraze.io/products/multi-ranger-deck/[accessed 26 August 2021].
83. M. Burri, M. Bloesch, Z. Taylor, R. Siegwart, J. Nieto, A framework for maximum likelihood parameter identification applied on mavs. *J. Field Robot.* **35**, 5–22 (2018).
84. T. Oktay, C. Sultan, Robustness of variance constrained controllers for complex, control oriented helicopter models, in *2013 American Control Conference* (IEEE, 2013), pp. 794–799.
85. E. J. Smeur, Q. Chu, G. C. de Croon, Adaptive incremental nonlinear dynamic inversion for attitude control of micro air vehicles. *J. Guid. Control Dynam.* **39**, 450–461 (2016).
86. E. R. Ulrich, *Design, Developement, Analysis and Control of a Bio-Inspired Robotic Samara Rotorcraft* (University of Maryland, College Park, 2012).
87. R. B. Bramlette, T. A. Johnston, R. M. Barrett-Gonzalez, Design, construction, and flight testing of the world's fastest micro-scale quadcopter, in *Proceedings of the 55th AIAA Aerospace Sciences Meeting* (AIAA, 2017), p. 0012.
88. DJI tello; https://store.dji.com/shop/tello-series[accessed 21 August 2021].
89. Parrot mambo; https://support.parrot.com/global/support/products/parrot-mambo[accessed 21 August 2021].

Acknowledgments: We thank X. Cai, H. Xie, S. Tan, and B. Mu for helpful discussions during the course of the project. We also thank H. Jia, R. Ding, K. Dong, and S. Zhong for assistance with the experiments. **Funding:** The work described in this paper was substantially supported by grants from the Research Grants Council of the Hong Kong Special Administrative Region, China (project nos. CityU 11207718 and CityU 11215220). **Author contributions:** S.B. and P.C. conceived the ideas and designed the study. S.B. designed, fabricated, and tested the prototypes. S.B. and P.C. analyzed and interpreted the results. Q.H. designed and implemented the experiments for characterizing the wings and propellers. P.C. and S.B. wrote and revised the manuscripts. **Competing interests:** The authors declare that they have no competing interests. **Data and materials availability:** All data needed to evaluate the conclusions in the article are present in the paper or the Supplementary Materials.

Submitted 15 January 2021
Accepted 14 April 2022
Published 11 May 2022
10.1126/scirobotics.abg5913

Science Robotics

A bioinspired revolving-wing drone with passive attitude stability and efficient hovering flight

Songnan Bai, Qingning He, and Pakpong Chirarattananon

Sci. Robot. **7** (66), eabg5913. DOI: 10.1126/scirobotics.abg5913

Science Robotics (ISSN 2470-9476) is published by the American Association for the Advancement of Science. 1200 New York Avenue NW, Washington, DC 20005. The title *Science Robotics* is a registered trademark of AAAS.